

Electronic Supplementary Information (ESI)

**Fibrous Thiazolothiazole-bridged Viologen Polymer for
High-Performance Lithium-Ion Batteries**

Ling Chen,^{‡a} Xiaolin Zhu,^{‡*a} Youzhi Zhang,^a Guangyuan Gao,^a Wenhao Xue,^a Sen Zhang,^a Xiujuan Wang,^a Qichun Zhang,^b and Xiaoming He^{a*}

a. Key Laboratory of Applied Surface and Colloid Chemistry of Ministry of Education, School of Chemistry of Chemical Engineering, Shaanxi Normal University, Xi'an 710119, P.R. China. E-mail: xiaolinchem@snnu.edu.cn; xmhe@snnu.edu.cn

b. Department of Materials Science and Engineering, City University of Hong Kong, Kowloon, Hong Kong, 999077, China

[‡] These authors contributed equally to this work

*Corresponding Author Email: xiaolinchem@snnu.edu.cn; xmhe@snnu.edu.cn

Experimental Section

Materials and Instruments.

Poly(1,1-difluoroethylene) (PVDF) ($M_w = 534,000$), *N*-methyl-2-pyrrolidinone (NMP) and carbon black (ECP-600JD) were purchased from Shenzhen Kejing Zhida Technology Co., Ltd. Lithium chip, electrolyte, CR2032 battery case and separator were purchased from DoDoChem. Tetrabutylammonium hexafluorophosphate (TBAPF₆) was purchased from Sigma-Aldrich and recrystallized from EtOH before drying under vacuum before use. All other chemical reagents were purchased from commercial sources (Alfa Aesar, Energy-chemical and Adamas) and were used as received, unless otherwise noted.

The ¹H NMR spectra were recorded on a 400 MHz or 600 MHz Bruker spectrometer. The ¹³C NMR spectra were recorded at 100 MHz or 150 MHz. High resolution mass spectrometry (HRMS) data were collected on a Bruker maxis UHR-TOF mass spectrometer in ESI positive mode. The solid-state ¹³C NMR spectra were obtained on a JEOL RESONANCE ECZ 400R NMR spectrometer at a MAS rate of 12 kHz. Fourier transform infrared (FT-IR) measurements were carried out using a Bruker Tensor27 spectrophotometer. Powder X-ray diffraction (PXRD) patterns were recorded on Bruker D8 Advance instrument. Brunauer-Emmett-Teller (BET) surface area were measured by Micromeritics ASAP 2460 instrument. Thermo-gravimetric analyses (TGA) were carried out on TA (Q1000DSC+LNCS+FACS Q600SDT) instrument. Surface analyses by X-ray Photoelectron Spectroscopy (XPS) were collected on Kratos AXIS ULTRA. Scanning electron microscope (SEM) images were obtained using a Hitachi SU8220. Transmission electron microscopy (TEM) and HR-TEM images were acquired using FEI (Tecnai G2 F20) instrument. Ultraviolet-visible (UV-vis) absorption spectra were recorded on Cary 3500 spectrometer. Emission spectra and the absolute quantum yield were carried out on Horiba FluoroMax Plus spectrofluorometer. X-ray single crystal diffraction data were collected on a Nonius Kappa CCD diffractometer, using Mo K α radiation (λ) 0.71073 Å (graphite monochromator).

Synthesis of 2,5-bis(4-pyridyl)thiazolo[5,4-d]thiazole (Py₂TTz).

Py₂TTz was synthesized according to the previous reported procedure, and the data of ¹H NMR spectrum was matched the literature^{S1}. ¹H NMR (400 MHz, CDCl₃): δ (ppm) = 8.78 (d, J = 6.0 Hz, 4H; H₂), 7.88 (d, J = 6.0 Hz, 4H; H₁).

Synthesis of diaryliodonium triflate

Diaryliodonium triflate was synthesized according to the previous reported procedure from Olofsson group^{S2}.

General synthetic procedure for compounds 1-3.

Py₂TTz (90.0 mg, 0.3 mmol), copper(II) acetate (6.0 mg, 0.03 mmol) and diaryliodonium triflate (1.2 mmol) were heated to 100 °C in 10 mL of DMF for 36 h under nitrogen condition. The reaction solution was then cooled to RT and poured into 50 mL of CH₂Cl₂. The product was isolated by centrifugation, followed with washed several times with CH₂Cl₂ and ether.

***N,N'*-diphenyl 2,5-bis(4-pyridinium)thiazolo[5,4-d]thiazole ditriflate (1).** Yellow solid, yield: 89%. ¹H NMR (400 MHz, DMSO-*d*₆): δ (ppm) = 9.52 (d, *J* = 6.0 Hz, 4H; H₅), 8.90 (d, *J* = 6.0 Hz, 4H; H₄), 7.95 (s, 4H; H₃), 7.79 (s, 6H; H₁₊₂). ¹³C NMR (100 MHz, DMSO-*d*₆): δ (ppm) = 165.54, 156.24, 146.98, 146.37, 142.78, 131.92, 130.71, 125.06, 124.49, 122.68, 119.48. ESI-HRMS (*m/z*): calcd for [C₂₆H₁₈N₄S₂]²⁺, 225.0481; found, 225.0486.

***N,N'*-di(1-(4-bromophenyl)) 2,5-bis(4-pyridinium)thiazolo[5,4-d]thiazole ditriflate (2).** Yellow solid, yield: 85%. ¹H NMR (400 MHz, DMSO-*d*₆): δ (ppm) = 9.50 (d, *J* = 6.0 Hz, 4H; H₄), 8.92 (d, *J* = 6.4 Hz, 4H; H₃), 8.04 (d, *J* = 8.8 Hz, 4H; H₂), 7.93 (d, *J* = 8.8 Hz, 4H; H₁). ¹³C NMR (100 MHz, DMSO-*d*₆): δ (ppm) = 165.57, 156.39, 147.18, 146.43, 141.93, 133.58, 127.35, 125.49, 124.50, 122.72, 119.52. ESI-HRMS (*m/z*): calcd for [C₂₆H₁₆Br₂N₄S₂]²⁺, 303.9576; found, 303.9587.

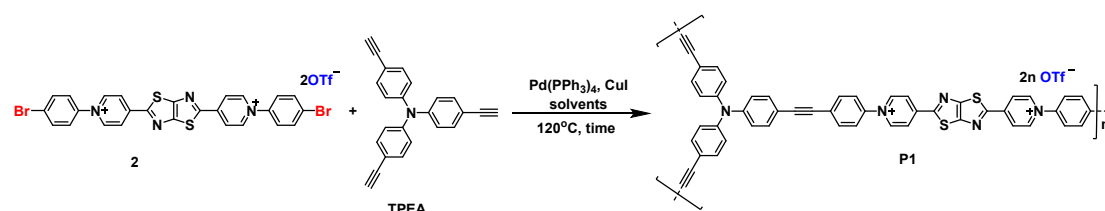
***N,N'*-di(1-(4-methoxyphenyl)) 2,5-bis(4-pyridinium)thiazolo[5,4-d]thiazole ditriflate (3).** Yellow solid, yield: 85%. ¹H NMR (400 MHz, DMSO-*d*₆): δ (ppm) = 9.46 (d, *J* = 7.2 Hz, 4H; H₅), 8.86 (d, *J* = 7.2 Hz, 4H; H₄), 7.91 (d, *J* = 9.2 Hz, 4H; H₃), 7.33 (d, *J* = 9.2 Hz, 4H; H₂), 3.91 (s, 6H; H₁). ¹³C NMR (100 MHz, DMSO-*d*₆): δ (ppm) = 165.57, 161.86, 156.16, 146.40, 146.10, 135.86, 126.46, 124.45, 122.73, 119.52, 115.77, 56.47. ESI-HRMS (*m/z*): calcd for [C₂₈H₂₂N₄O₂S₂]²⁺, 255.0587; found, 255.0588. **Crystal Data** for C₁₅H₁₁F₃N₂O₄S₂ (*M* = 404.38 g/mol): monoclinic, space group C2/c, *a* = 16.4424(12) Å, *b* = 10.2099(8) Å, *c* = 20.8080(15) Å, β = 110.745(2), *V* = 3266.7(4) Å³, *Z* = 8, *T* = 153.0 K, μ (CuK α) = 3.515 mm⁻¹, *D*_{calc} = 1.644 g/cm³, 24564 reflections measured (9.088° ≤ 2 θ ≤ 136.608°), 2978 unique (*R*_{int} = 0.0473, *R*_{sigma} = 0.0271) which were used in all calculations. The final *R*₁ was 0.0276 (*I* > 2 σ (*I*)) and *wR*₂ was 0.0781 (all data).

Synthesis of *N,N'*-dibenzyl 2,5-bis(4-pyridinium)thiazolo[5,4-d]thiazole dibromide (4).

The compound was synthesized by using a procedure modified from a literature¹. **Py₂TTz** (296 mg, 1.0 mmol) and benzyl bromide (1.37 g, 8.0 mmol) were heated to 90 °C for 2 days in 30 mL dry DMF under nitrogen condition. The product was isolated by centrifugation, following washed several times with CH₂Cl₂ to afford bright yellow solid (Yield: 63%). ¹H NMR (600 MHz, DMSO-*d*₆): δ (ppm) = 9.36 (d, *J* = 7.2 Hz, 4H; H₅), 8.79 (d, *J* = 7.2 Hz, 4H; H₆), 7.59 (d, *J* = 7.2 Hz, 4H; H₃), 7.49-7.45 (m, 6H; H₁₊₂), 5.92 (s, 4H; H₄).

Optimization of experimental conditions for synthesis of **P1**.

We have optimized synthetic conditions of **P1** by screening stoichiometric ratios, various solvent mixtures and reaction time, meanwhile keeping other experimental conditions the same. We found that the polymerization in a mixture of Et₃N/toluene (1:1.5, v/v) solvent is optimal to afford resilient mesoporous fibrous **P1** (see Figure S13).



Stoichiometric ratio	Solvents (mL)	Time (h)	Stirring bar	Morphology
1.5:1	Toluene/Et ₃ N = 1.5 / 1	48	Without	Fig. S13a
1.5:1	DMF/Et ₃ N = 1.5 / 1	48	Without	Fig. S13b
1.5:0.8	Toluene/Et ₃ N = 1.5 / 1	48	Without	Fig. S13c
1:0.8 (optimal)	Toluene/Et ₃ N = 1.5 / 1	48	Without	Fig. S13d
1:0.8	Toluene/Et ₃ N = 1.5 / 1	48	With	Fig. S13e
1:0.8	Toluene/Et ₃ N = 1.5 / 1	72	Without	Fig. S13f

Synthesis of **P1** (optimal condition).

Under nitrogen condition, compound **3** (17.6 mg, 0.02 mmol), tris(4-ethynylphenyl)amine (8.0 mg, 0.025 mmol), Pd(PPh₃)₄ (1.5 mg, 5%) and CuI (0.5 mg, 10%) were heated to 120 °C for 48 h in a solvent mixture of Et₃N/toluene (2.5 mL, 1:1.5, v/v) without stirring. After cooling to room temperature, the precipitate was collected by centrifugation and washed with CH₃OH, CH₂Cl₂ and ether, respectively, for several times. A dark brown powder was obtained after vacuum oven drying (Yield: 58%).

Synthesis of **P2-Br**.

Py₂TTz (296 mg, 1.0 mmol) and α,α' -dibromo-p-xylene (264 mg, 1.0 mmol) were heated to 90 °C for 3 days in 30 mL dry DMF under nitrogen condition. The product was isolated by centrifugation, which washed several times with CH₂Cl₂ to afford dark yellow solid (Yield: 99%).

Synthesis of P2.

P2 (1.0 mmol) and methyl trifluoromethanesulfonate (10 mol) were stirred at RT overnight in 30 mL dry CH₃CN under nitrogen condition. After removing the solvent by evaporation, the product was washed several times with CH₂Cl₂ to afford orange yellow solid (Yield: 99%).

Cyclic Voltammetry of 1-4.

Cyclic voltammetry (CV) curves were performed on a CHI760E instrument. CV experiments of the small molecules were conducted on a 0.5 mM solution in degassed DMF containing 0.05 M TBAPF₆ as supporting electrolyte. A typical three-electrode cell was used having a polished glassy carbon (with 4 mm diameter) electrode as the working electrode, a Pt-wire as the counter electrode, and Ag/AgCl as the reference electrode, potential E referenced to Fc⁺/Fc.

Spectroelectrochemical Methods.

The solution for spectroelectrochemical experiment were prepared in CH₃CN without degassing and other conditions were the same as above. A customized three-electrode electrolytic cell was used with a Pt-mesh electrode as the working electrode, a Pt-wire as the counter electrode, and Ag/AgCl electrode as the reference electrode. The voltage range and the time were controlled by the program of the electrochemical workstation, and the absorption spectra were recorded by UV-vis spectrophotometer.

Battery Fabrication and Testing.

The working electrode materials were prepared by mixing the active material, carbon black (ECP-600JD) and polyvinylidene fluoride in a mass ratio of 60/30/10 using *N*-methyl pyrrolidone as solvent. The electrodes were then prepared by casting the resulting inks onto carbon-coated copper foil. The fully prepared electrodes were dried at 50 °C for 6 h, and then kept at 80 °C overnight in a vacuum oven in order to remove residual solvent. The electrodes were cut into disks with a diameter of 12 mm, and the mass loading of active material pasted on the carbon-coated copper foil is about 0.4-0.7 mg cm⁻². CR2032-type coin cells were assembled in an argon-filled glove box (<0.1 ppm of oxygen and <0.01 ppm of water). Lithium foil was employed as the counter electrode and macroporous polypropylene separator film (Celgard 2400) was

adopted as the separator. 1.0 M LiPF₆ in a mixture of ethylene carbonate (EC), dimethyl carbonate (DMC) and ethyl methyl carbonate (EMC) (1:1:1, v/v/v) with 1% vinylene carbonate (VC) was used as the electrolyte. The batteries were stood for 12 h before testing.

The battery performance was collected on the LAND CT2001A battery system at various current densities within the voltage window of 0.005-3.0V at room temperature. The cyclic voltammetry measurements of batteries were performed on the CHI760 electrochemical workstation. The electrochemical impedance spectroscopy (EIS) was tested at a frequency range of 100 kHz to 0.1 Hz.

Theoretical specific capacity calculation.

The theoretical specific capacity of the electrode materials is calculated according to the following formula:

$$Q = \frac{nF}{3.6M_w}$$

Q: theoretical specific capacity (mAh g⁻¹), n: the number of transferred electrons from one molecule or one repeating unit, F: Faraday constant (96500 C mol⁻¹), and M_w: molecular weight of one molecule or one repeating unit (g mol⁻¹).

In our work, **P1**: M_w(repeating unit)=2868.81 g mol⁻¹, n(repeating unit)=6, and **P2**: M_w(repeating unit)=698.64 g mol⁻¹, n(repeating unit)=2, thus the theoretical specific capacity of **P1** is 56 mAh g⁻¹ and **P2** is 77 mAh g⁻¹.

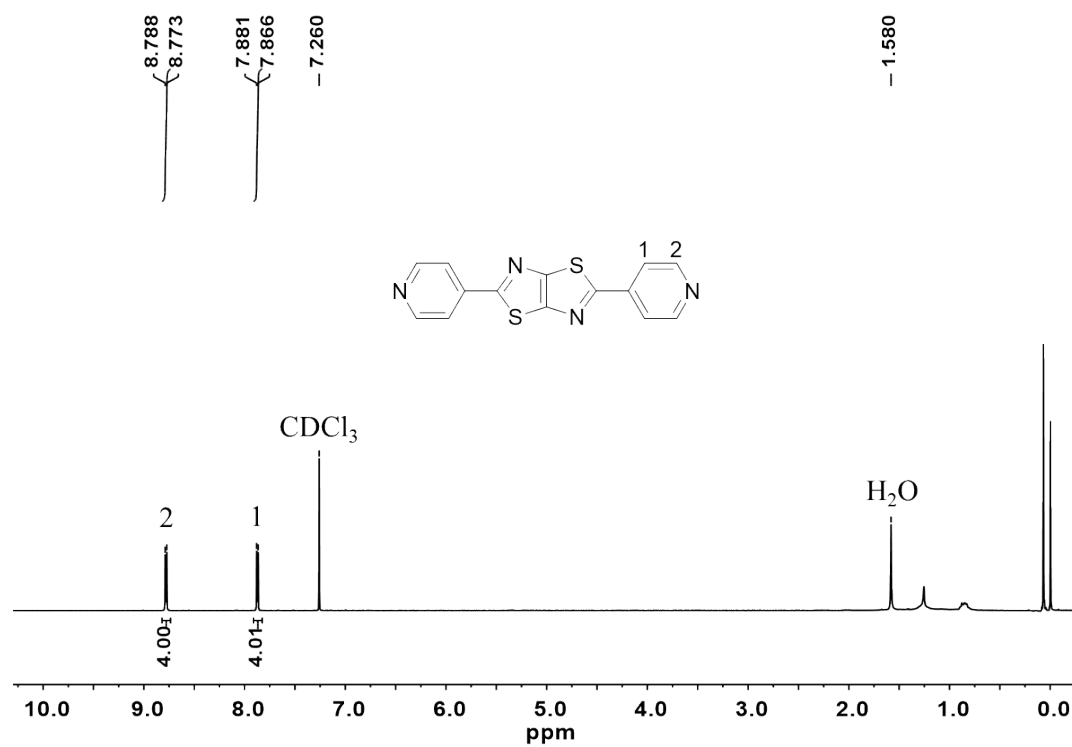


Figure S1. ¹H NMR spectrum (400 MHz) of **Py₂TTz** in CDCl₃.

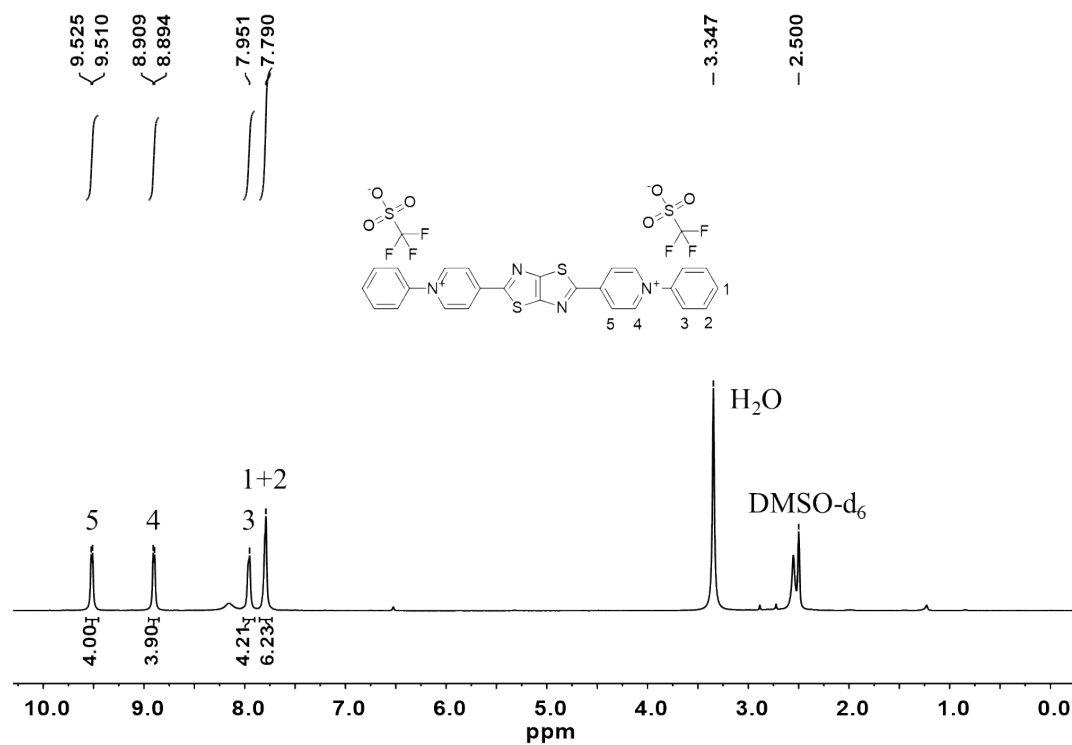


Figure S2. ¹H NMR spectrum (400 MHz) of **1** in DMSO-*d*₆.

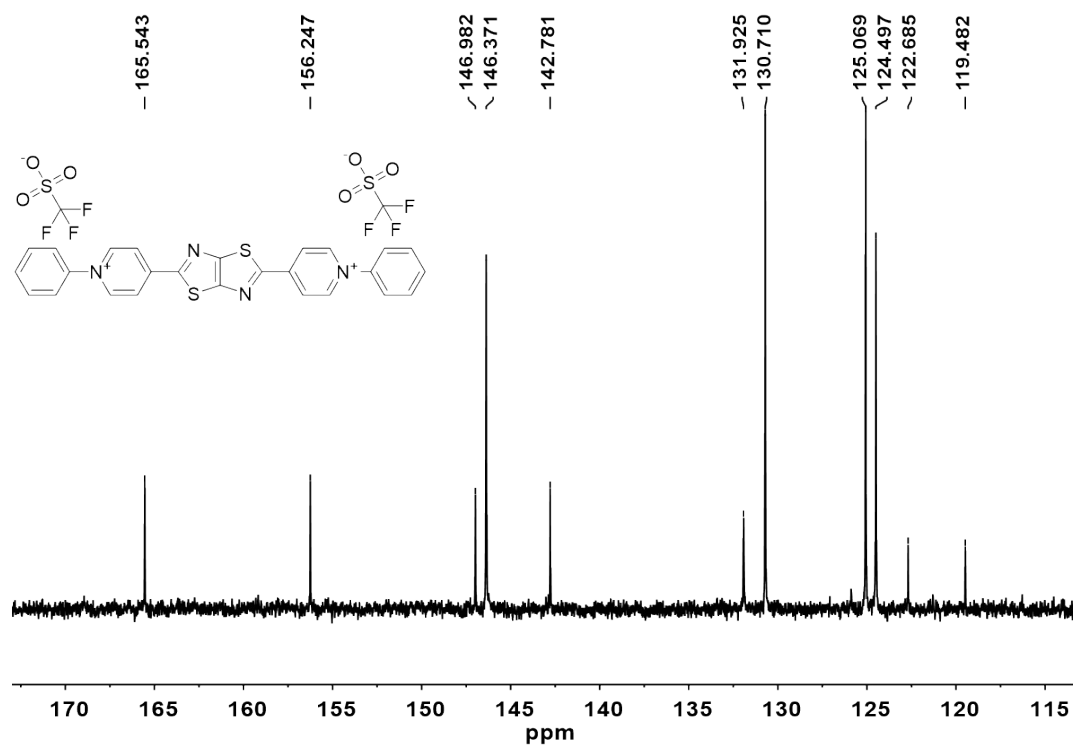


Figure S3. ¹³C NMR spectrum (100 MHz) of **1** in DMSO-*d*₆.

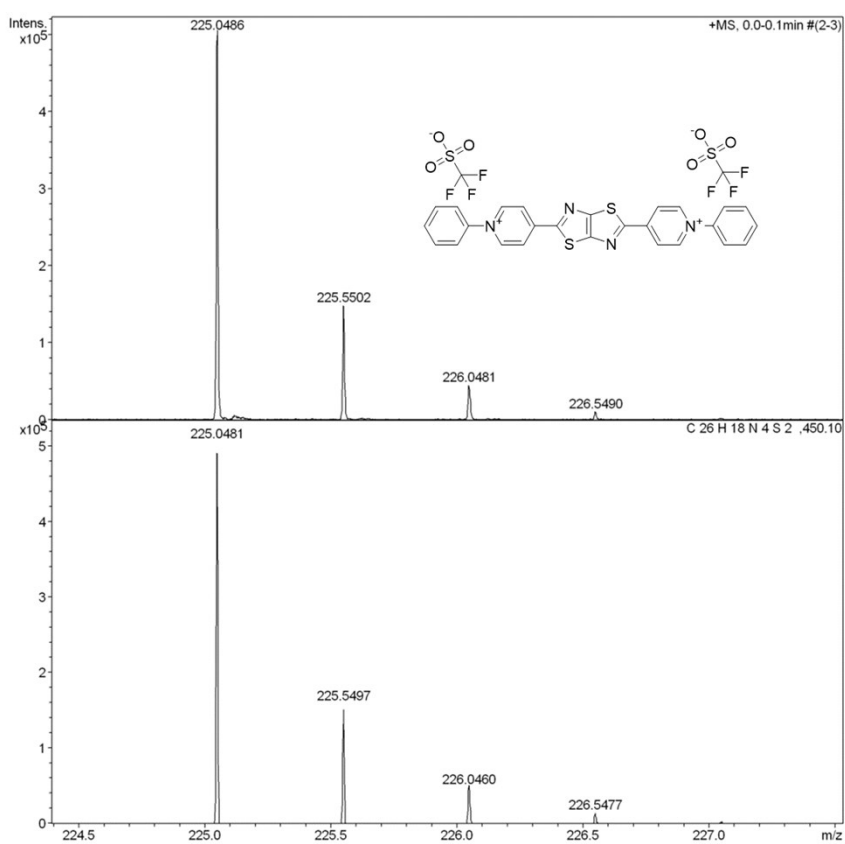


Figure S4. ESI-HRMS spectrum of **1**.

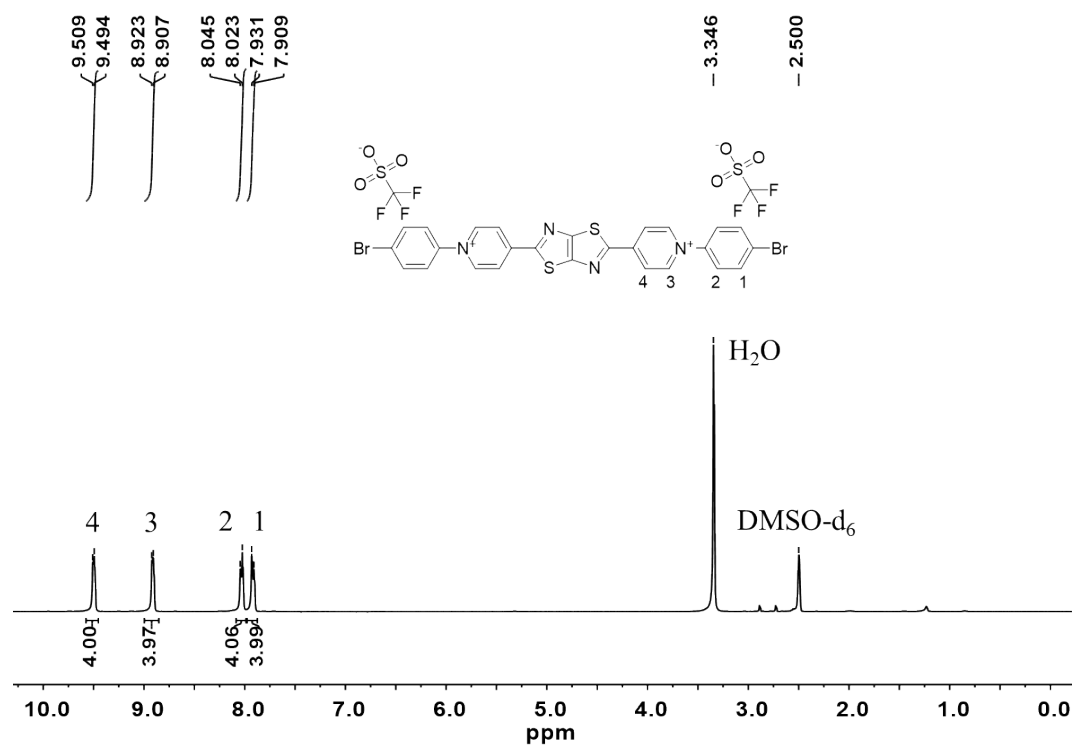


Figure S5. ¹H NMR spectrum (400 MHz) of **2** in DMSO-*d*₆.

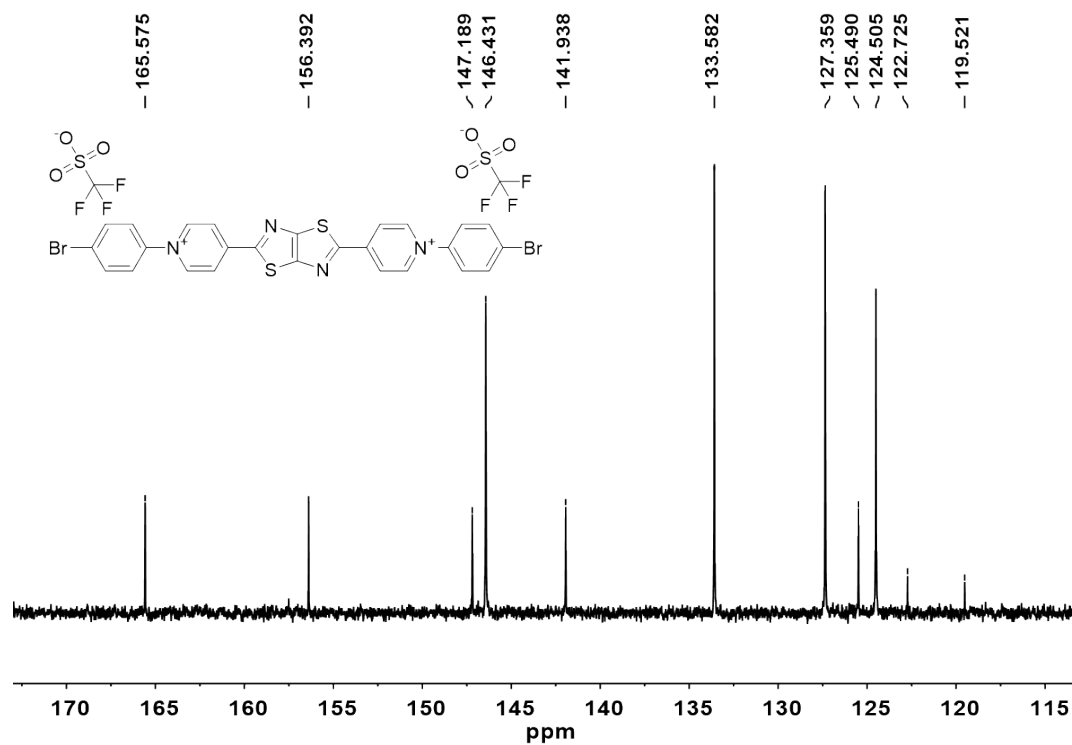


Figure S6. ¹³C NMR spectrum (100 MHz) of **2** in DMSO-*d*₆.

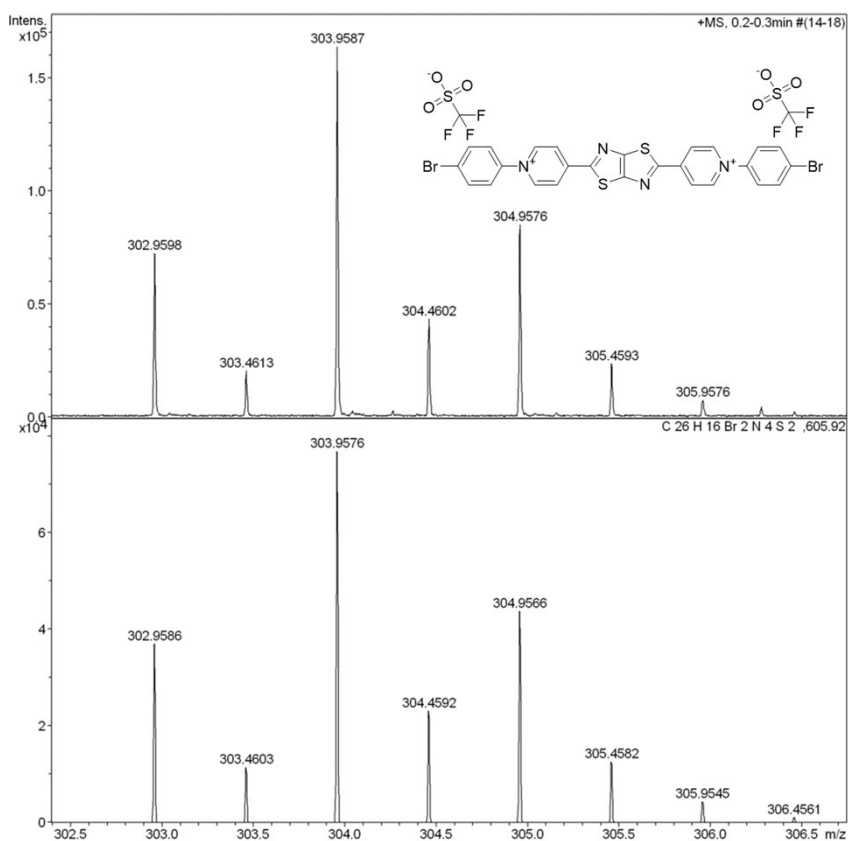


Figure S7. ESI-HRMS spectrum of **2**.

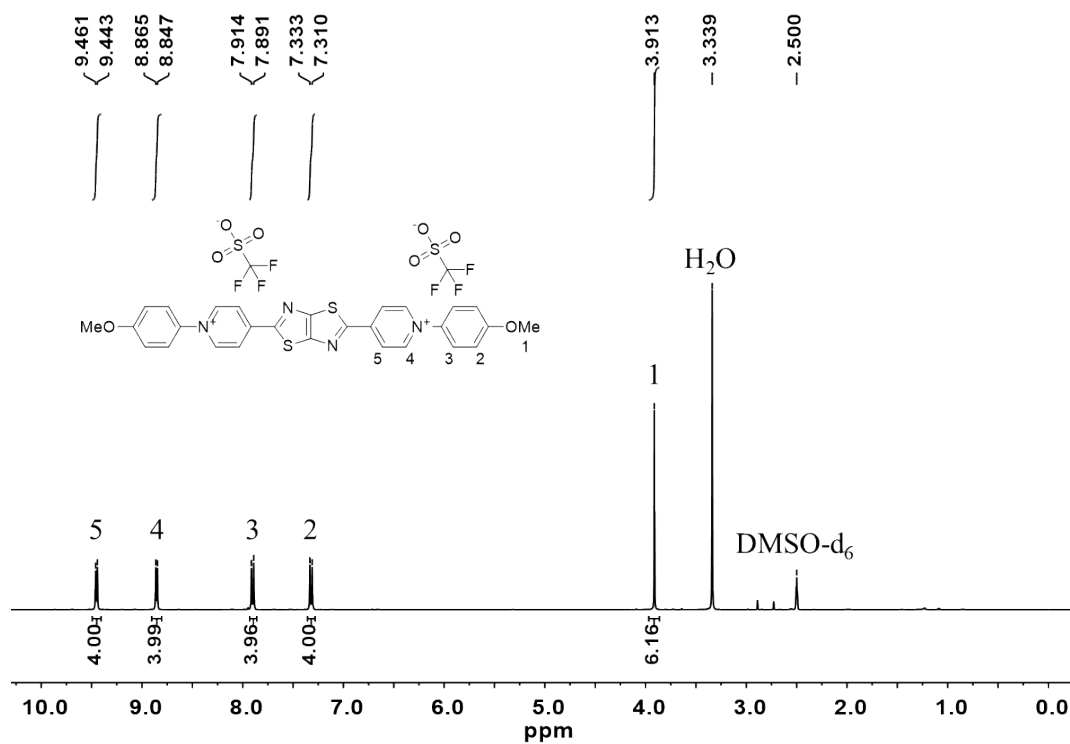


Figure S8. 1H NMR spectrum (400 MHz) of **3** in $DMSO-d_6$.

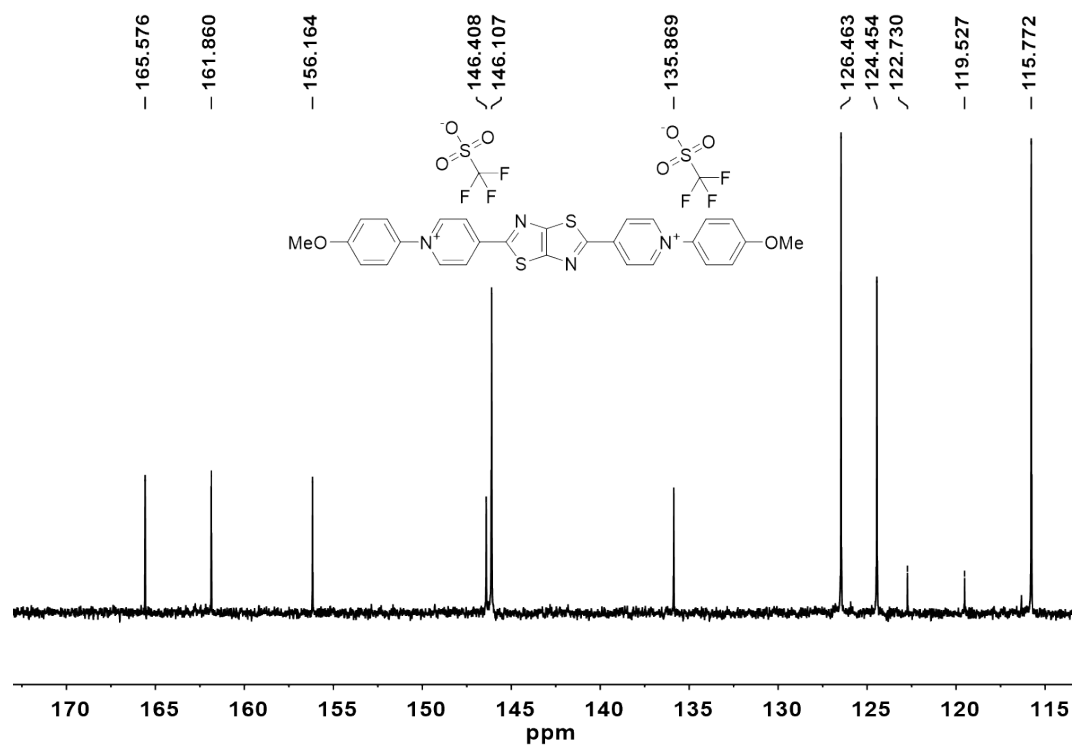


Figure S9. ^{13}C NMR spectrum (100 MHz) of **3** in $\text{DMSO}-d_6$.

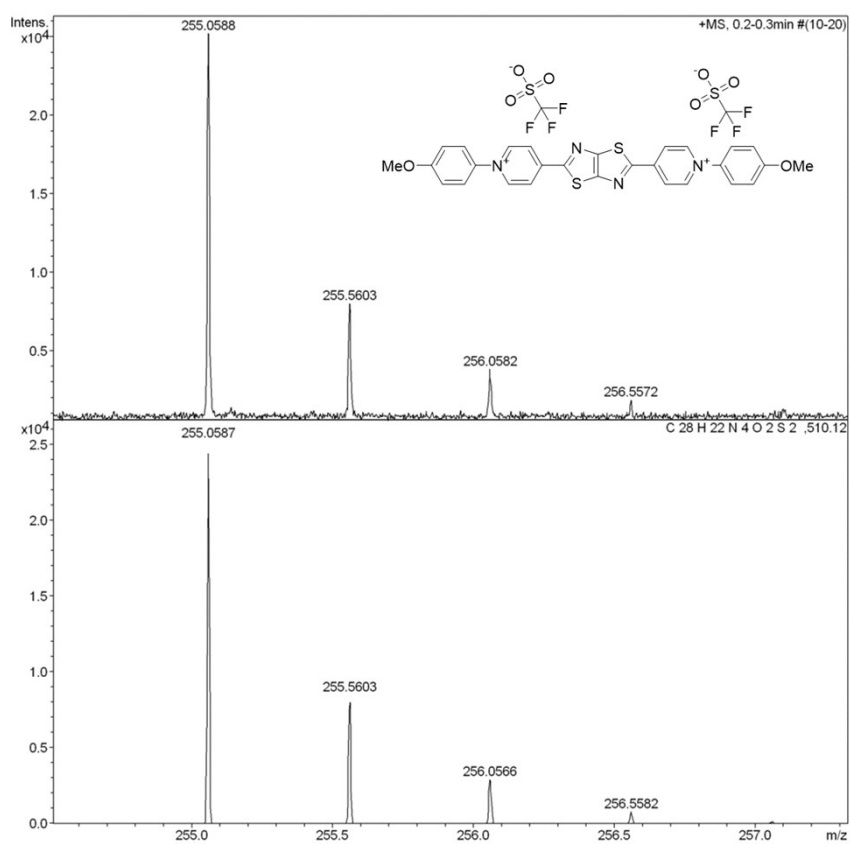


Figure S10. ESI-HRMS spectrum of **3**.

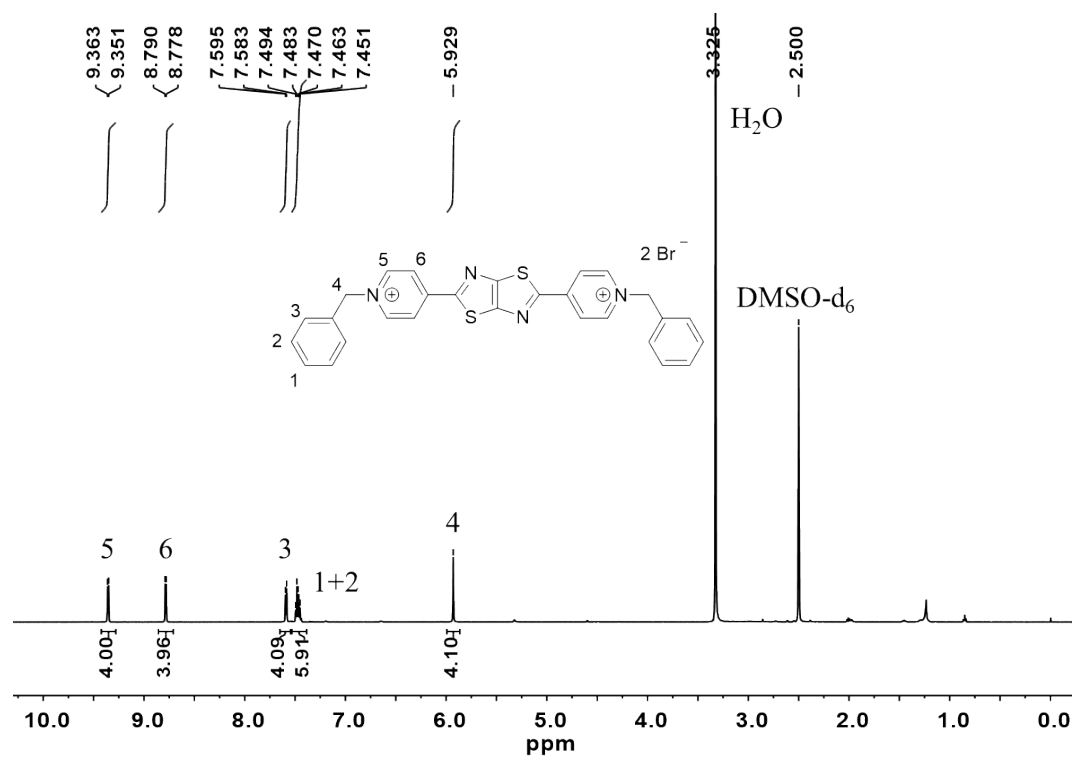


Figure S11. ¹H NMR spectrum (600 MHz) of **4** in DMSO-*d*₆.

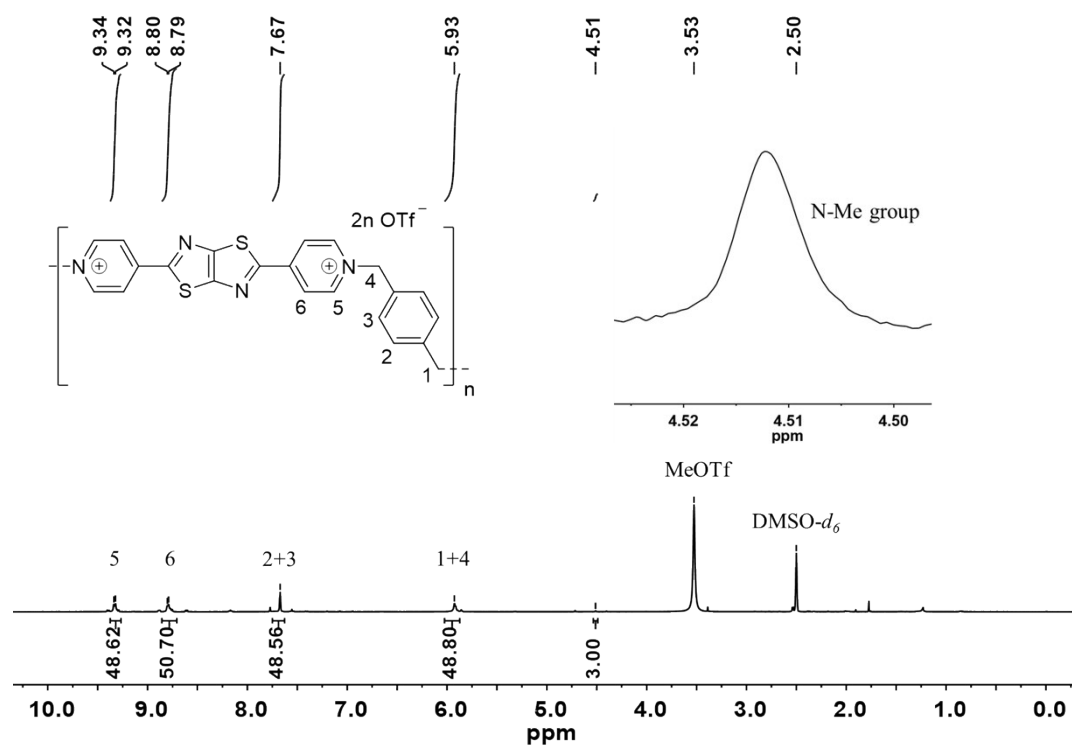


Figure S12. ^1H NMR spectrum (400 MHz) of **P2** in $\text{DMSO-}d_6$.

The chemical shift of N-methyl group at the end of **P2** is assigned to 4.51 ppm, and its hydrogen number is scaled to 3. In each repeating unit, the number of H atoms on α -pyridine is about 48. The signal ratio of N-Me group and α -H on pyridine in ^1H NMR shows that the degree of polymerization was *ca.* 12. Thus the molecular weight of **P2** is estimated to *ca.* 8400 g mol^{-1} .

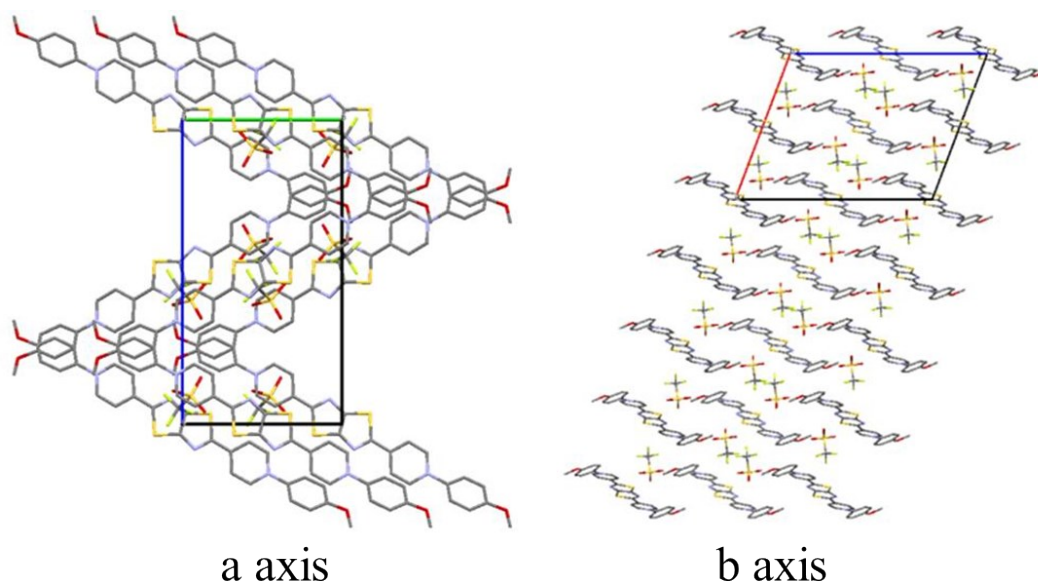


Figure S13. Molecular packing in crystals of **3** (CCDC 2071615).

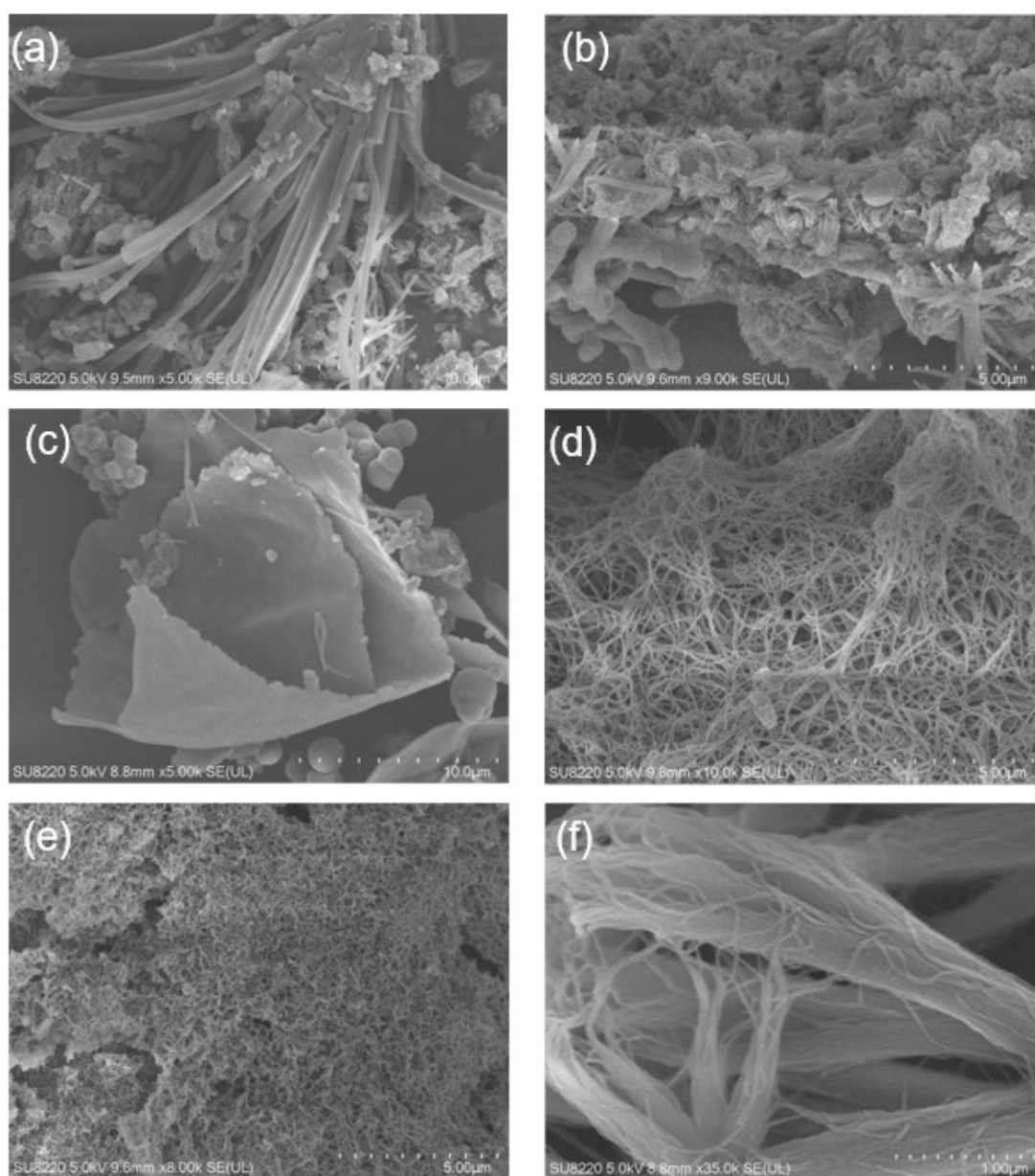


Figure S14. SEM images of **P1** obtained from various reaction conditions.

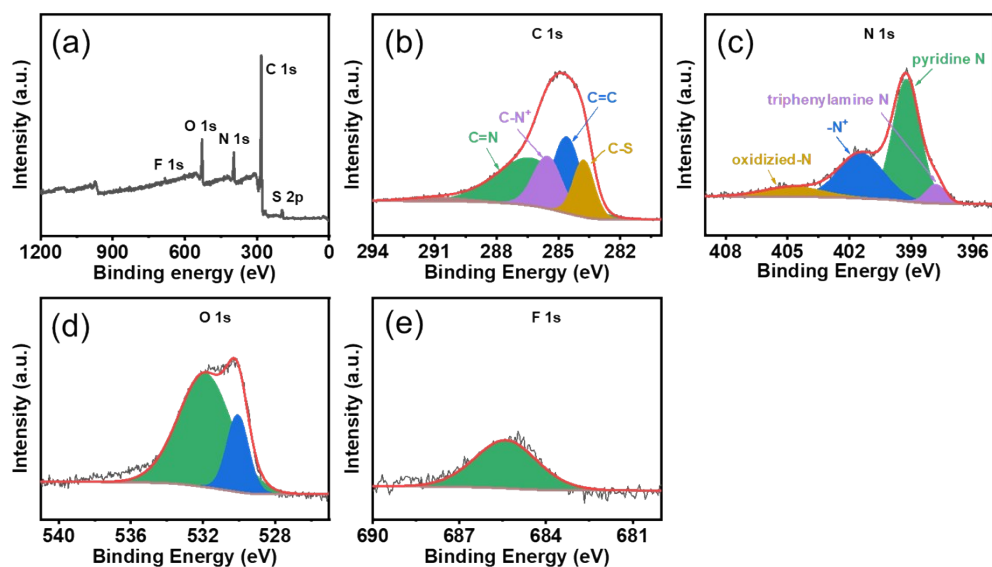


Figure S15. (a-e) XPS spectra of **P1**.

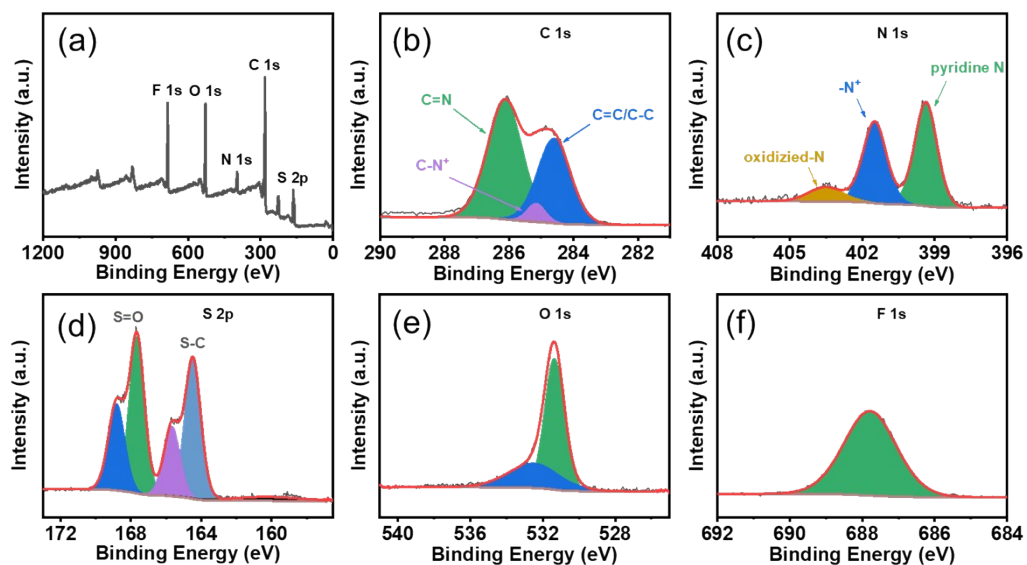


Figure S16. (a-f) XPS spectra of **P2**.

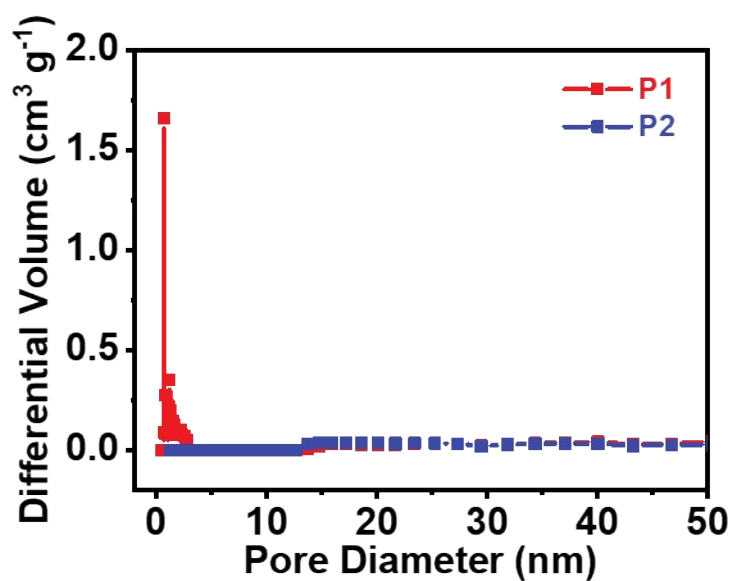


Figure S17. The pore-size distributions (0-50 nm) of **P1** and **P2**.

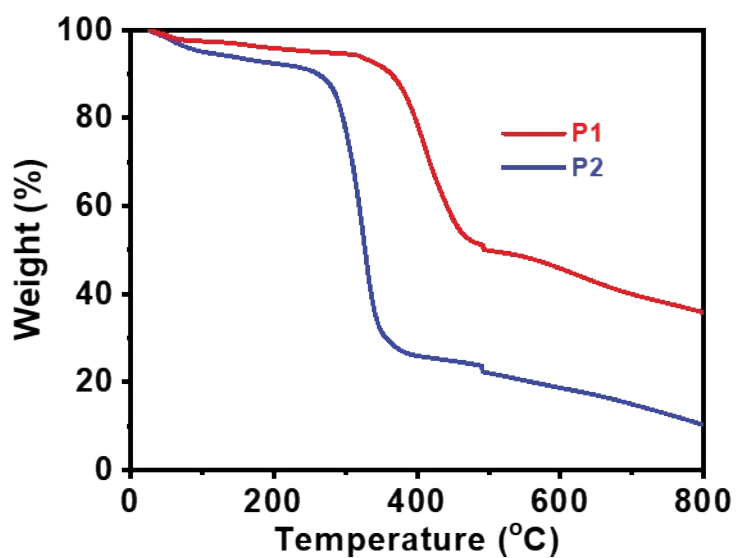


Figure S18. TGA profiles of **P1** and **P2** under nitrogen atmosphere.

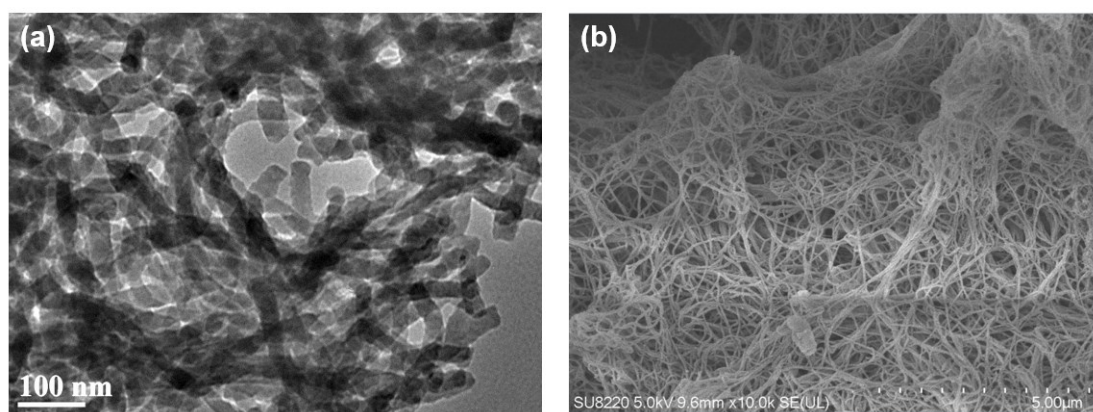


Figure S19. (a) TEM and (b) SEM image of **P1**.

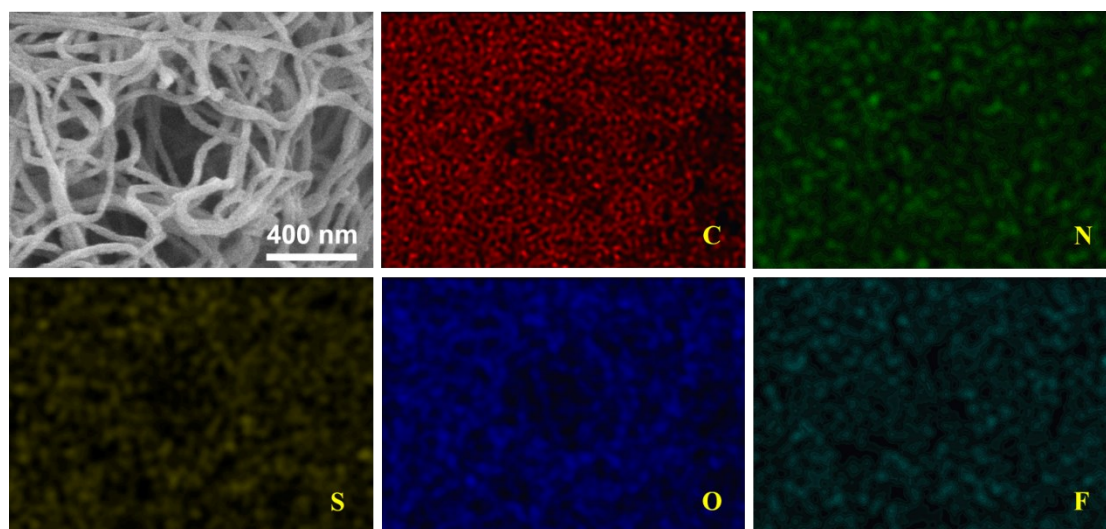


Figure S20. SEM element mapping images of **P1**.

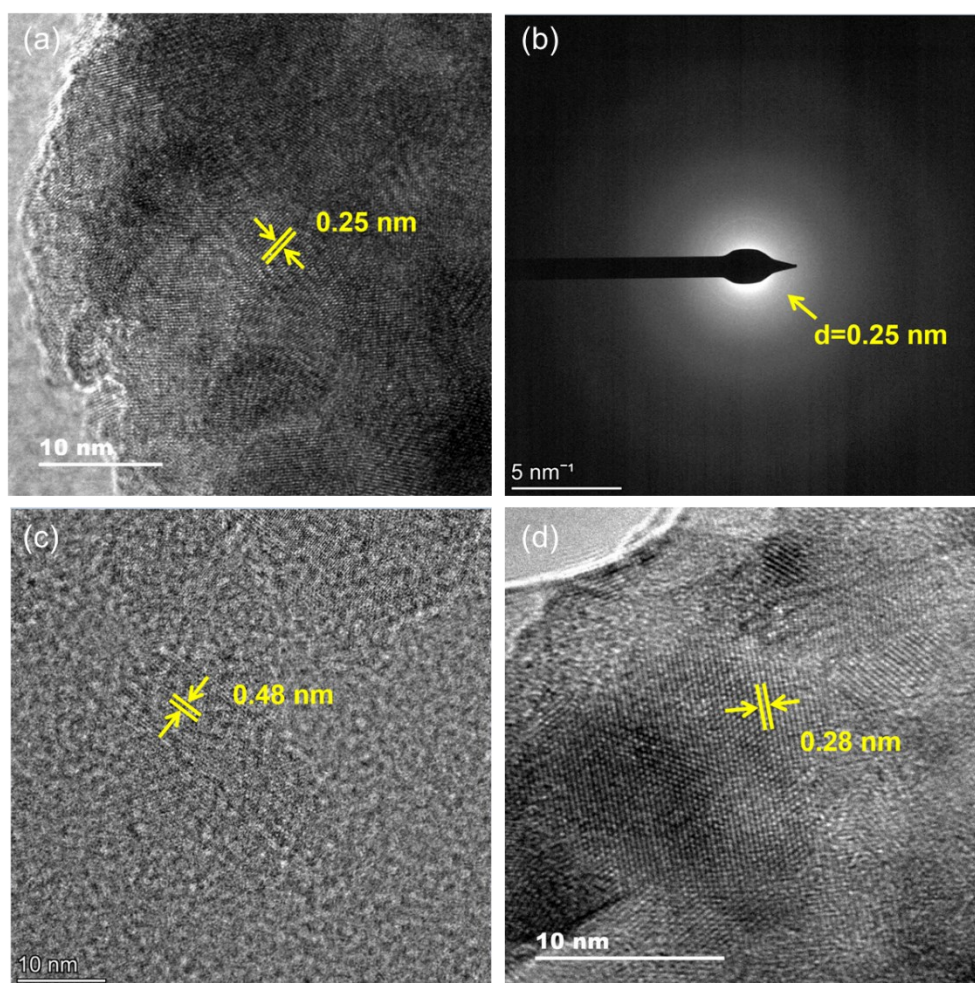


Figure S21. (a, c, d) HRTEM and (b) Selected Area Electron Diffraction (SAED) of P1.

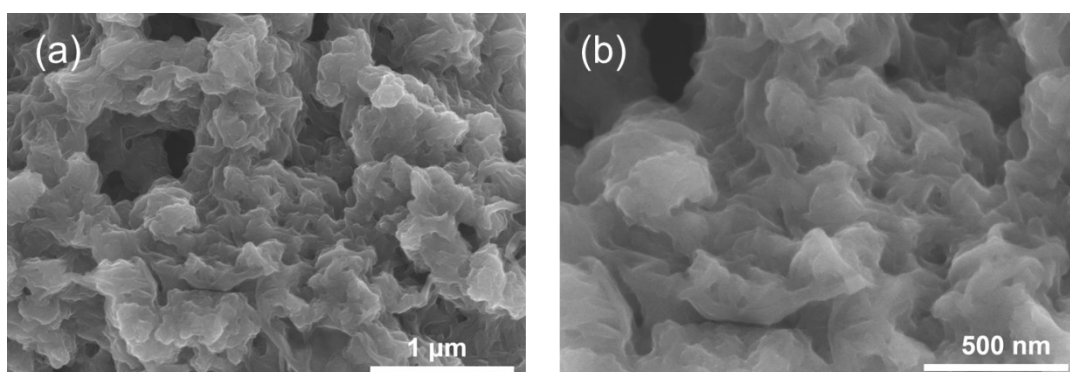


Figure S22. (a-b) SEM image of **P2**.

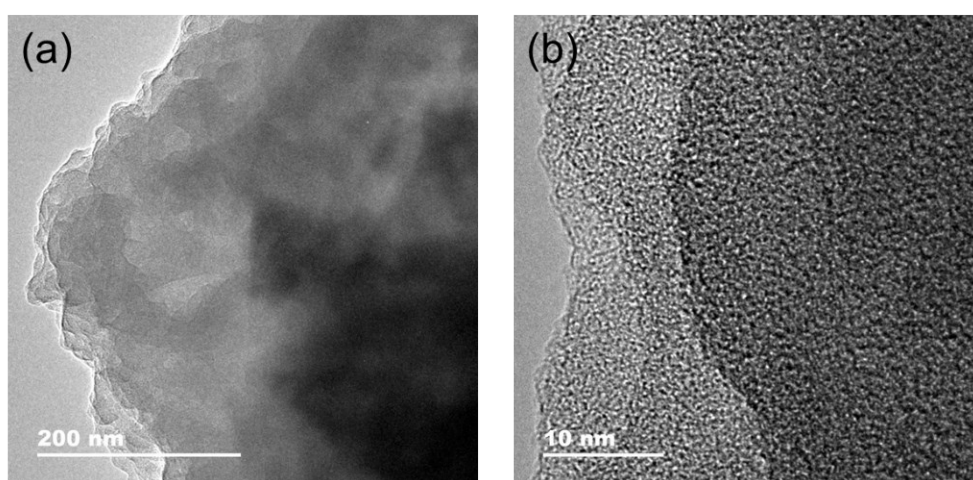


Figure S23. TEM image (a) and HRTEM (b) image of **P2**.

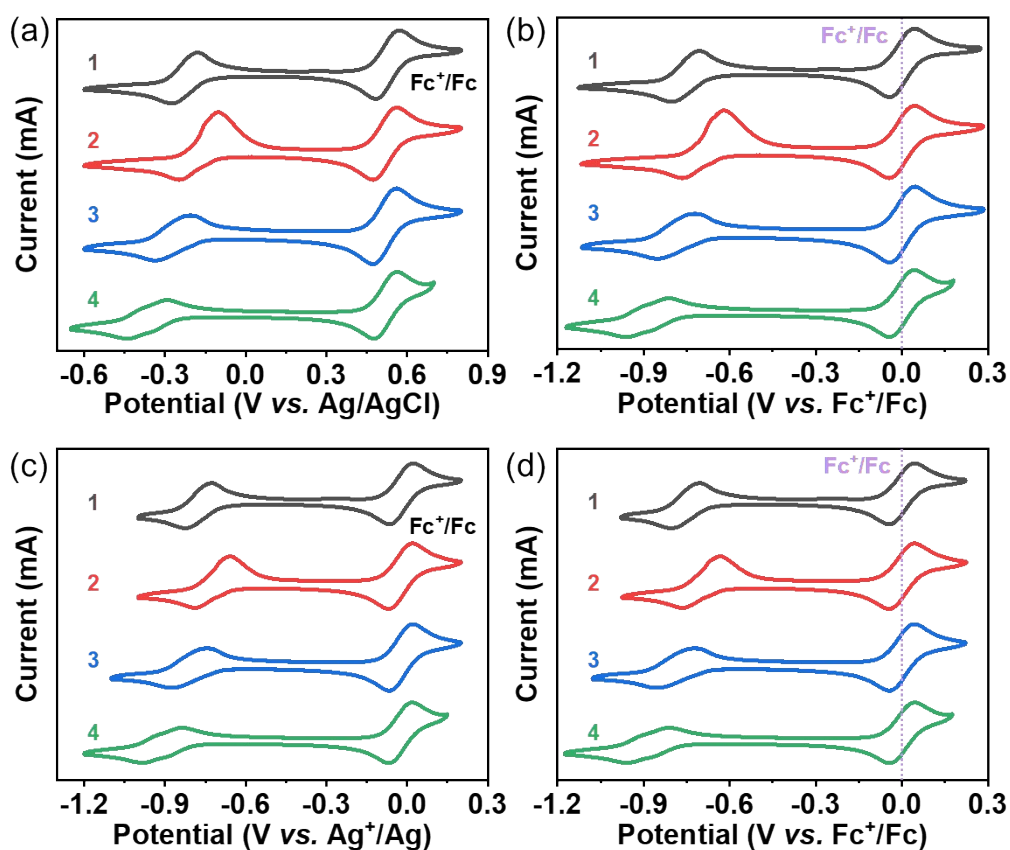


Figure S24. Cyclic voltammograms of 1-4 at 100 mV s⁻¹ in DMF solution with 0.05 M TBAPF₆ as supporting electrolyte by: (a) using Ag/AgCl as quasi-reference electrode and adding ferrocene; (b) using Ag/AgCl as quasi-reference electrode, potential E referenced to Fc⁺/Fc (defined E_{1/2}(Fc⁺/Fc)=0); (c) using Ag⁺/Ag as quasi-reference electrode and adding ferrocene; (d) using Ag⁺/Ag as quasi-reference electrode, potential E referenced to Fc⁺/Fc (defined E_{1/2}(Fc⁺/Fc)=0).

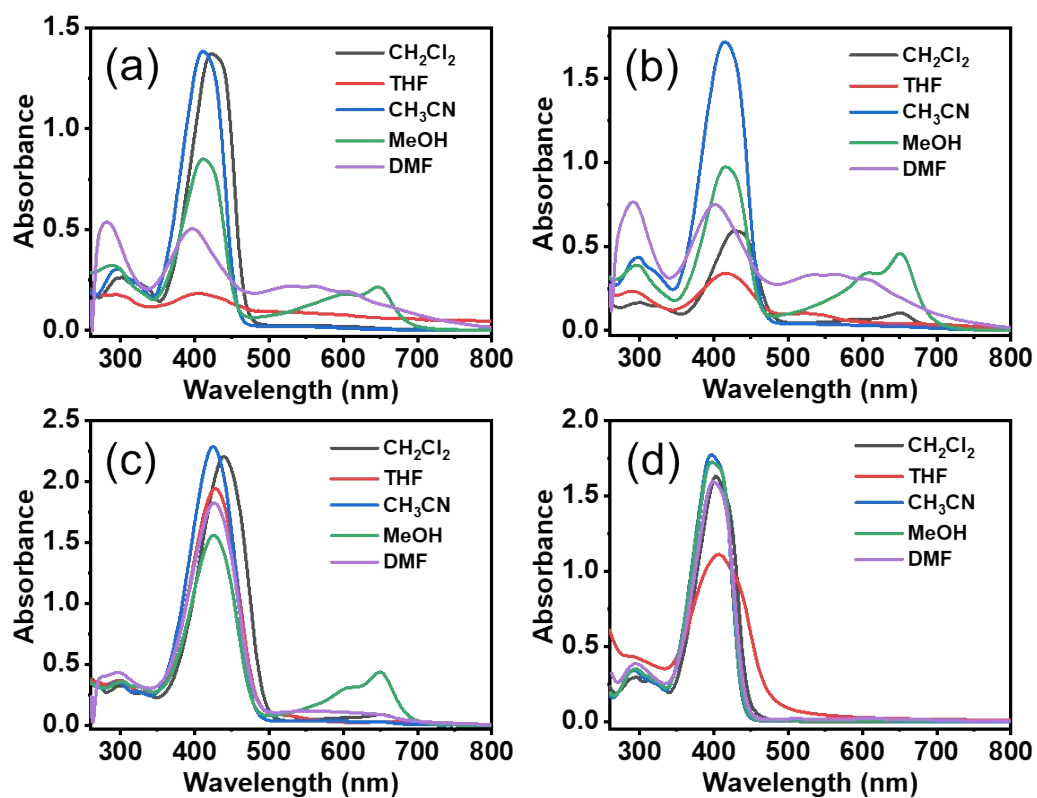


Figure S25. UV-vis absorption spectra of **1** (a), **2** (b), **3** (c), **4** (d) in different solvents, respectively.

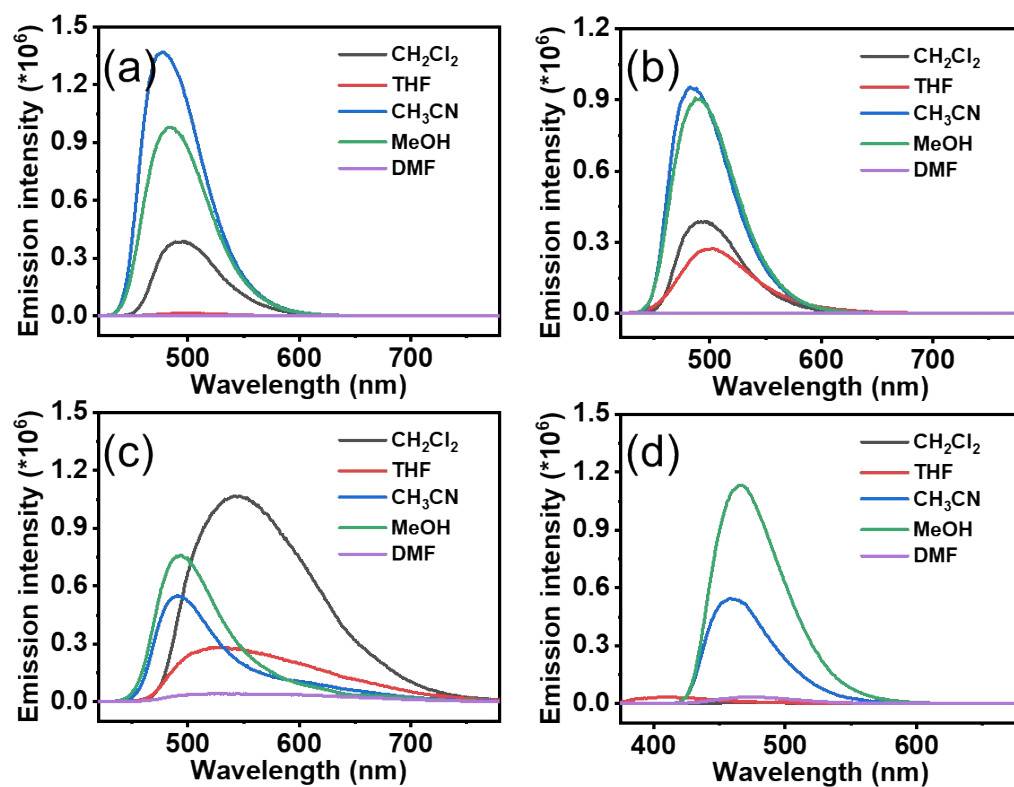


Figure S26. Emission spectra of **1** (a), **2** (b), **3** (c), **4** (d) in different solvents, respectively.

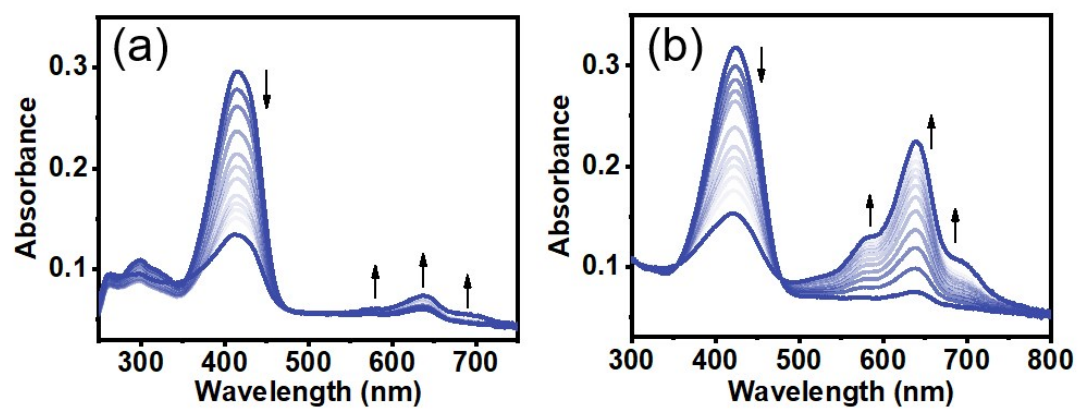


Figure S27. Spectroelectrochemistry of **2** (a) and **3** (b) in CH₃CN vs Ag/AgCl reference, respectively.

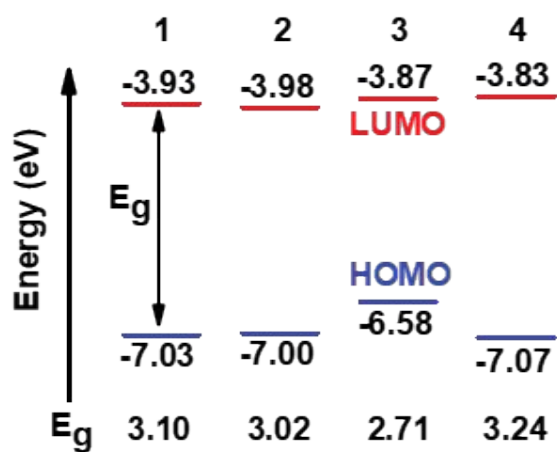


Figure S28. The molecular orbital surfaces of the HOMOs and LUMOs of **1-4** obtained at B3LYP/6-31G(d) level in CH_3CN .

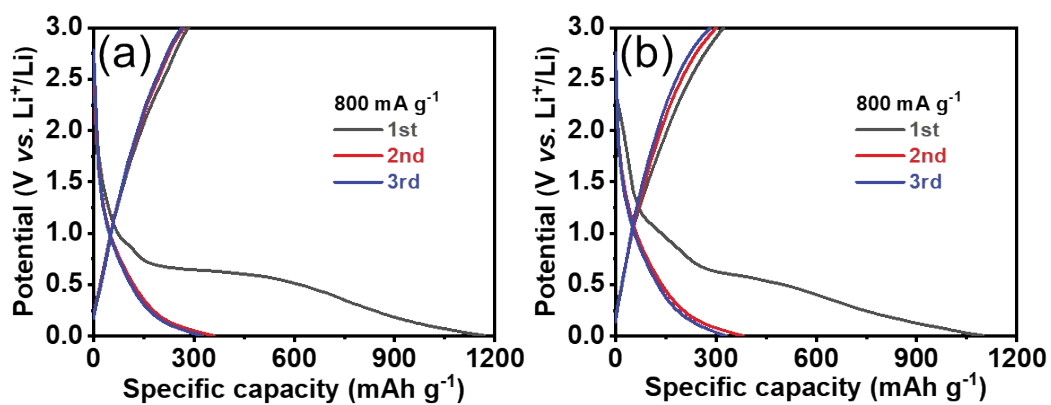


Figure S29. The first three charge-discharge profiles of **P1** (a) and **P2** (b) at a current density of 800 mA g^{-1} .

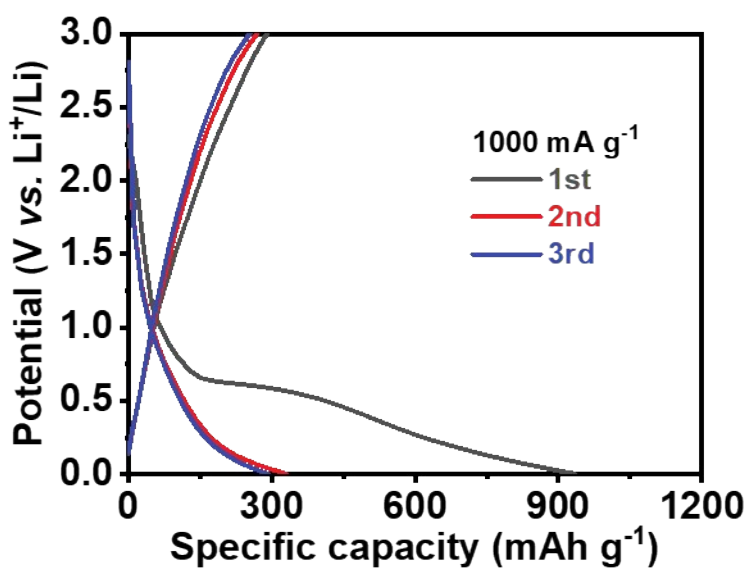


Figure S30. The first three charge-discharge profiles of **P1** at a current density of 1000 mA g^{-1} .

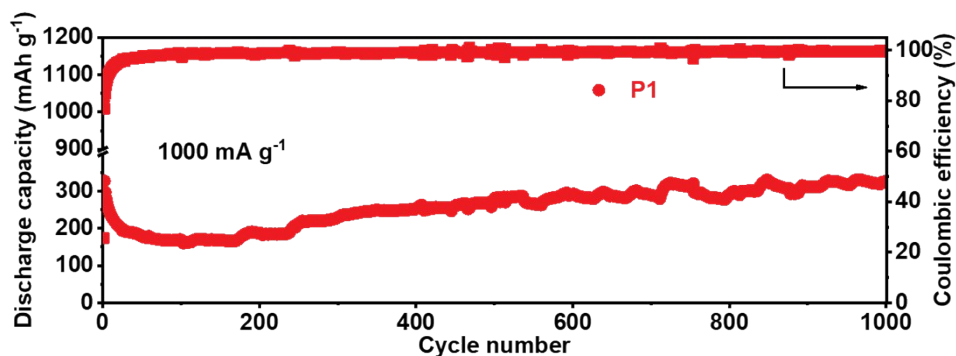


Figure S31. Long-term cycling property of **P1** at a current density of 1000 mA g⁻¹.

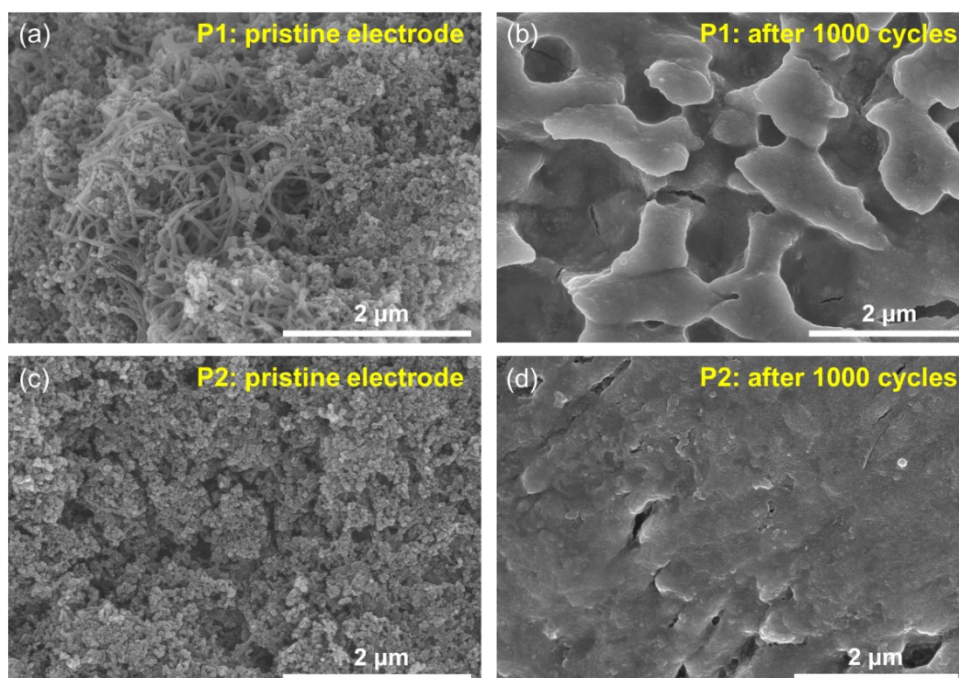


Figure S32. The ex-situ SEM images of **P1**: (a) pristine electrode, (b) after 1000 cycles; **P2**: (c) pristine electrode, (d) after 1000 cycles.

In SEM images, the uniform nanofibers mixed with carbon black are clearly observed for fresh **P1** electrode. Compared with the pristine electrode, it was observed that a lamellar film formed on the surface of **P1** electrode after long time of high current density cycling. This is due to the formation of SEI film and a consequence of continuous deposition of the electrolyte decomposed products during 1000 cycles^{S3}. But the lamellar structure on the surface of the electrode may enhance the kinetics of **P1**^{S4}. Similar changes were also observed for **P2** electrode. It formed a large plate on the surface of the electrode.

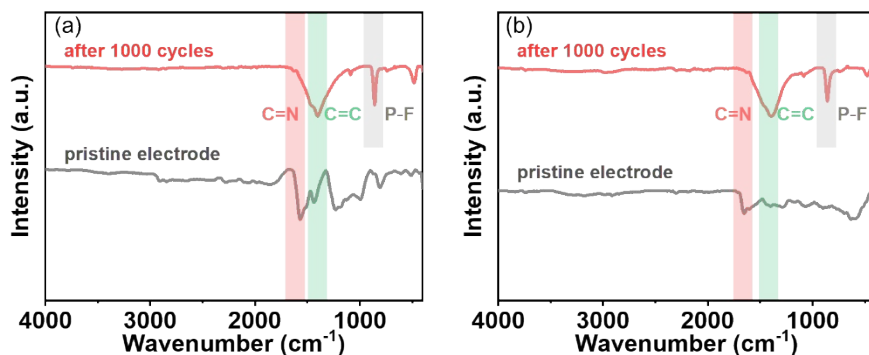


Figure S33. The ex-situ FT-IR spectra of (a) **P1** electrode and (b) **P2** electrode.

In FT-IR spectra of **P1** and **P2** pristine electrodes, the peaks at around 1600 cm^{-1} and 1400 cm^{-1} can be attributed to C=N bond from pyridine rings and C=C bond from benzene rings, respectively^{S5}. After 1000 cycles, both electrodes of **P1** and **P2** exhibit similar profile to that of pristine ones, indicating relatively good reversibility. In addition, the strong peak appears at about 860 cm^{-1} after cycling, which could be assigned to P-F bond of LiPF_6 ^{S6}.

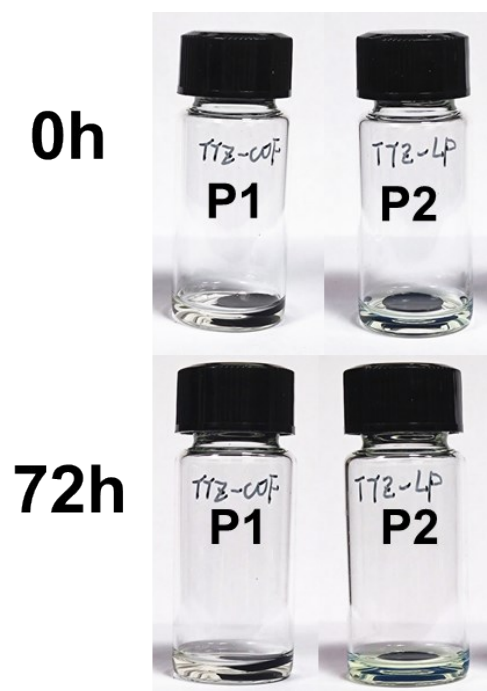


Figure S34. Solubility test of **P1** and **P2**.

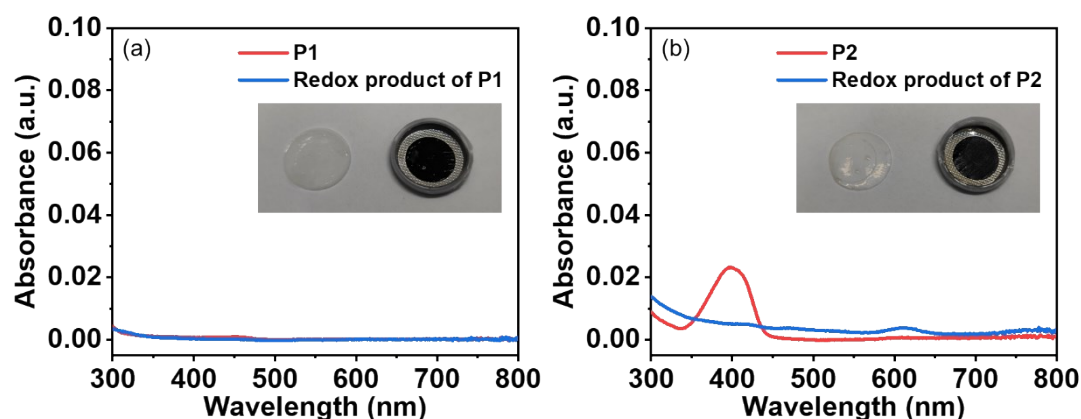


Figure S35. (a-b) UV-vis absorption spectra of **P1**, **P2** and their redox products in the electrolyte (EC: DMC: EMC=1:1:1 (v/v/v) with 1% VC) (Inset: Pictures of separator film and electrode of battery discharging to 0.005V).

Solution preparation: (1) Solubility test of **P1** and **P2**: The prepared electrodes with a loading of 0.5-0.8 mg cm⁻² were soaked in 2 mL electrolyte, and the upper-fluid were taken for UV-vis test; (2) Solubility test of redox products of **P1** and **P2**: After discharging the fresh battery to 0.005V, remove the electrode sheet and immerse it in 2 mL electrolyte. The test steps are the same as above. This is consistent with the photos of solubility test in **Fig. S34**.

UV-vis absorption spectroscopy showing extremely low solubility for **P1** and its reductive product in the electrolyte. In contrast, **P2** has a certain solubility in the electrolyte. There is a strong absorption peak at about 400 nm in UV-vis absorption spectra. The reduction product of **P2** can be detected as well, showing a new absorption peak at *ca.* 610 nm. In addition, the separator film of **P1** cell remains clean after discharge, while of **P2** cell has a slight stain. The results were consistent with UV-vis absorption spectra.

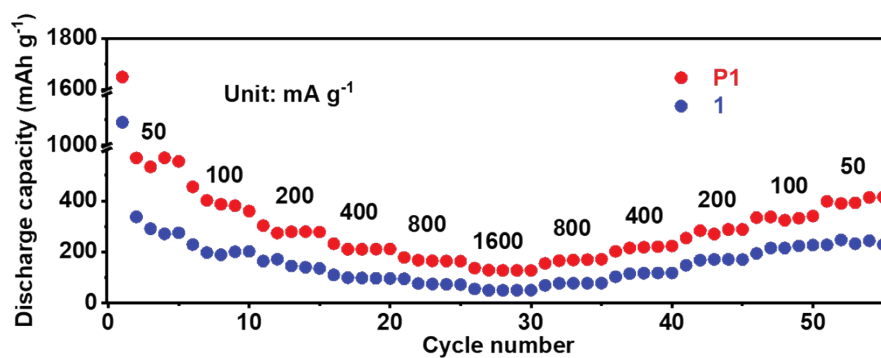


Figure S36. Rate performance for **1** and **P1**.

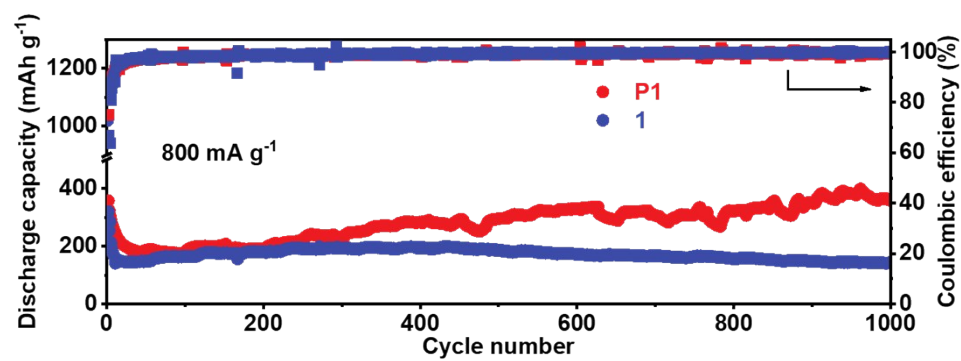


Figure S37. Long-term cycling property at 800 mA g^{-1} for **1** and **P1**.

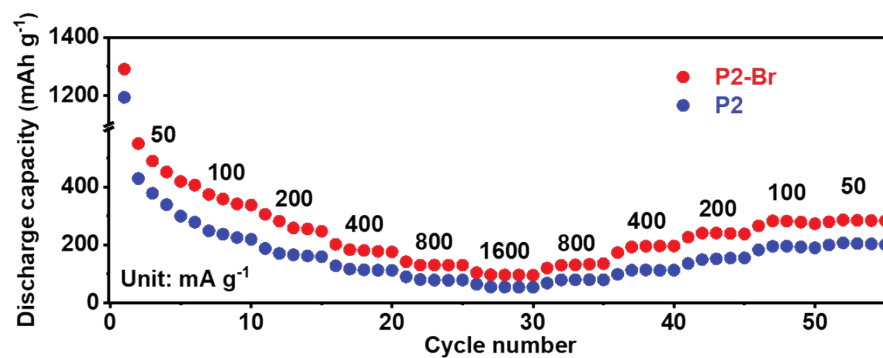


Figure S38. Rate performance for **P2** and **P2-Br**.

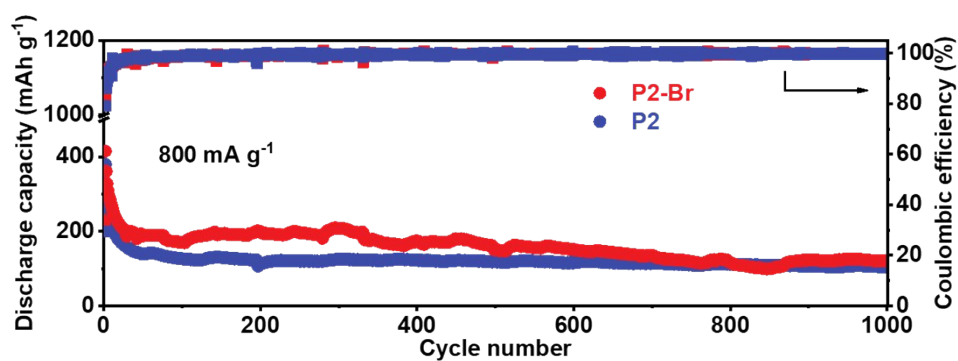


Figure S39. Long-term cycling property at 800 mA g^{-1} for **P2** and **P2-Br**.

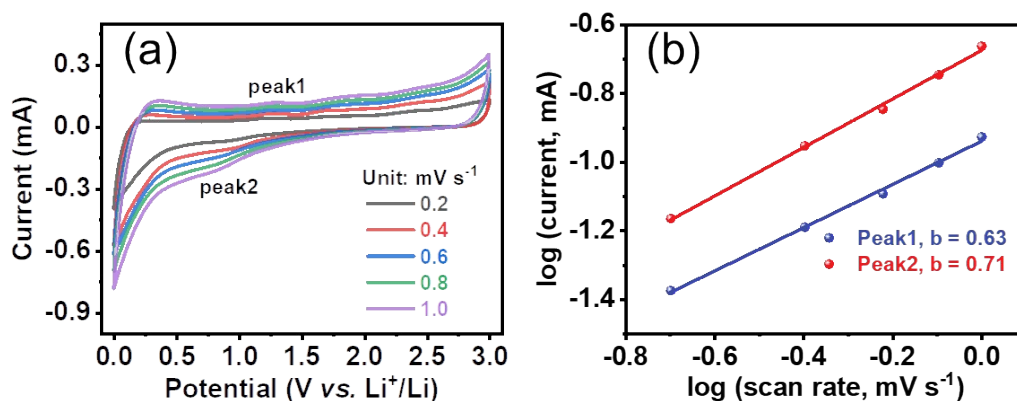


Figure S40. (a) CV curves of **P2** at different scan rates. (b) Log i versus log v plots of **P2** to determine the b values of different peaks.

The relation between measured peak current (i) and scan rate (v) obeys the following equations: $i = av^b$ and $\log(i) = b \times \log(v) + \log(a)$, where a and b are adjustable parameters. The value of b is very important as it can provide information about the types of the charge storage mechanism, which can be determined by the slope of the $\log(v)$ - $\log(i)$ plots. Specifically, if $b = 0.5$, the electrochemical process is an ideally diffusion-controlled behavior. When b equals to 1, there is an ideally capacitive process.

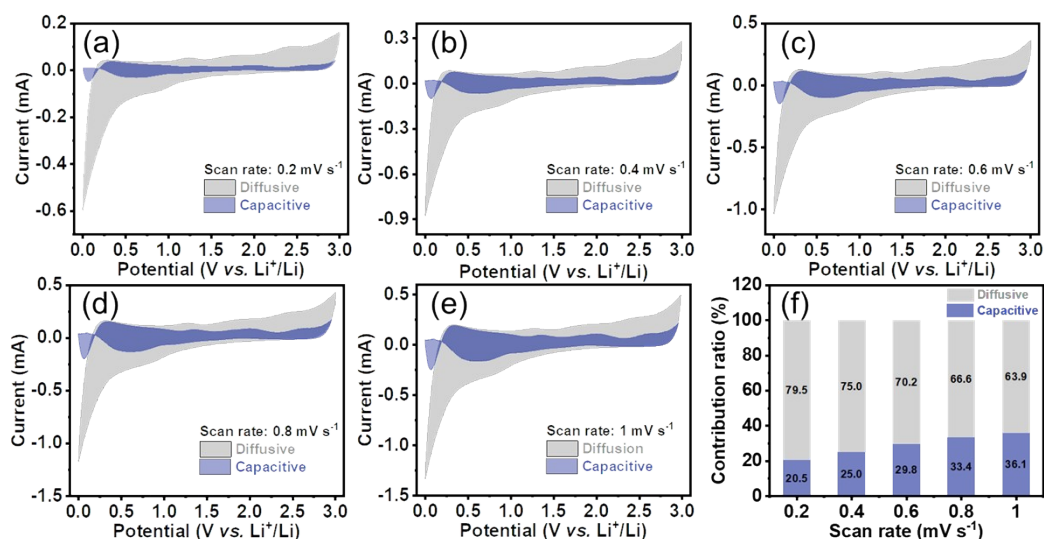


Figure S41. (a-e) Capacitive contribution of **P1** in CV curve at different scan rates. (f) The percentage contribution from capacitive and diffusive contribution of **P1**.

The specific percentage of capacitive and diffusive contribution can be further quantified by separating the current response (i) at a fixed potential (V) into capacitive contribution (k_1v) and diffusion-controlled contribution ($k_2v^{1/2}$) according to the equation: $i(V) = k_1(v) + k_2(v^{1/2})$, here k_1 and k_2 are constant for a given potential.

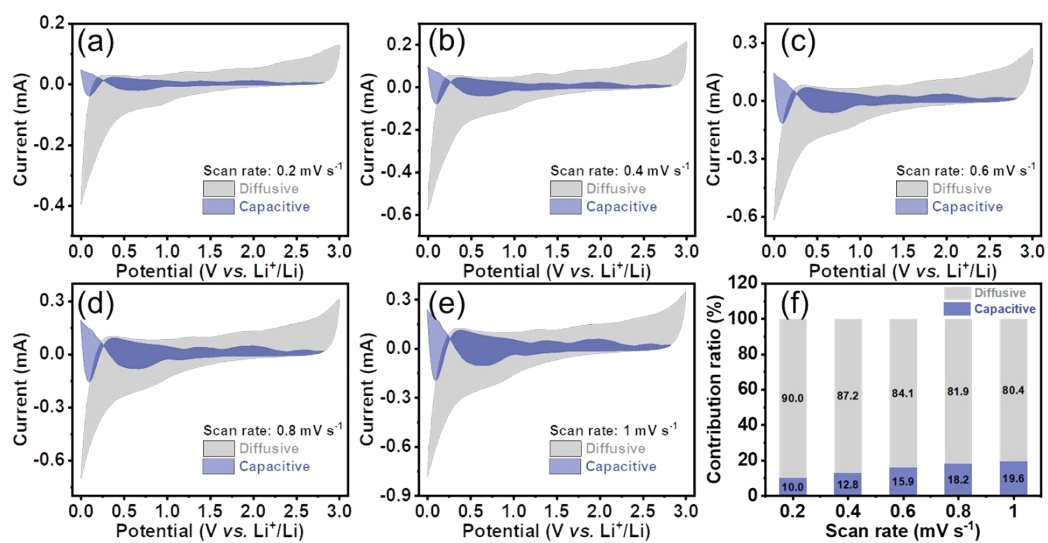


Figure S42. (a-e) Capacitive contribution of **P2** in CV curve at different scan rates. (f) The percentage contribution from capacitive and diffusive contribution of **P2**.

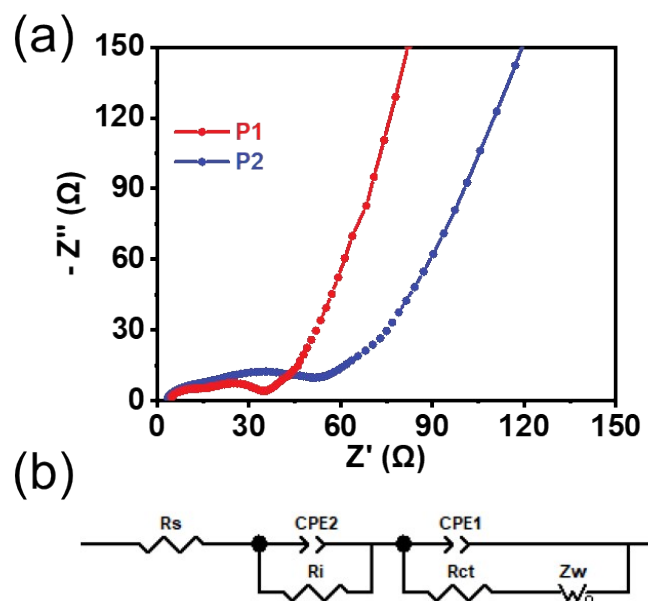


Figure S43. (a) Nyquist plots of **P1** and **P2** after 1000 cycles. (b) Equivalent circuit used for fitting the experimental data, where R_s , R_i , R_{ct} , CPE, and Z_w represent series resistance, interface resistance between electrolyte and deposited layer, charge-transfer resistance, constant-phase element, and Warburg diffusion process, respectively.

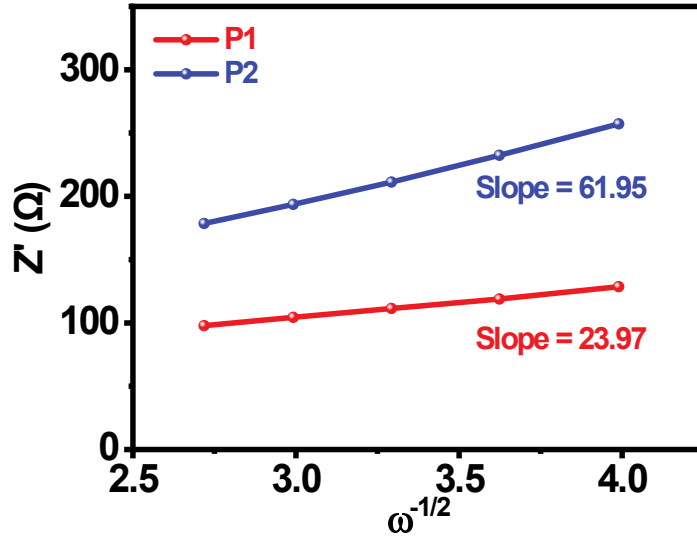


Figure S44. The relationship between real impedance in the low frequency range of **P1** and **P2** after 1000 cycles.

According to the equation: $Z' = R_e + R_{ct} + \sigma_w \omega^{-1/2}$ and $D_{Li^+} = \frac{R^2 T^2}{2 A^2 n^4 F^4 C^2 \sigma_w^2}$, the σ_w value is the Warburg factor, which can be obtained from the slope of $Z' - \omega^{-1/2}$ fitting line.

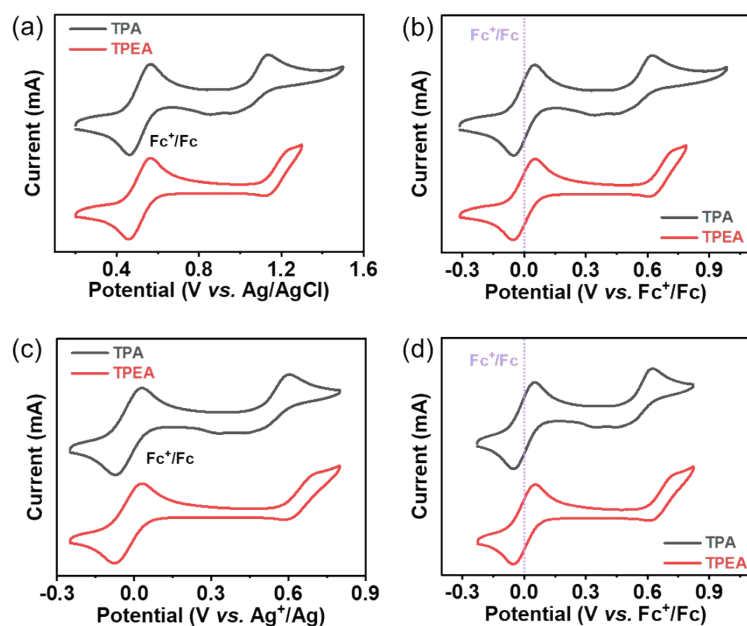


Figure S45. Cyclic voltammograms of tris(4-ethynylphenyl)-amine (TEPA) and triphenylamine (TPA) at 100 mV s^{-1} in DMF solution with 0.05 M TBAPF_6 as supporting electrolyte by: (a) using Ag/AgCl as quasi-reference electrode and adding ferrocene; (b) using Ag/AgCl as quasi-reference electrode, potential E referenced to Fc^+/Fc (defined $E_{1/2}(Fc^+/Fc)=0$); (c) using Ag^+/Ag as quasi-reference electrode and adding ferrocene; (d) using Ag^+/Ag as quasi-reference electrode, potential E referenced to Fc^+/Fc (defined $E_{1/2}(Fc^+/Fc)=0$).

Organic compounds can be categorized as n-type, p-type or bipolar according to their redox mechanisms^{S7-S8}. Most reported n-type organics including viologens first experience reduction, such as **P2** in our work, during which they combine with electrons and Li-ions. Conversely, p-type materials typically first undergo oxidation and must bind anions from the electrolyte to remain electroneutral. Triphenylamine derivatives are usually used as high-voltage ($>3.2\text{V}$, vs. Li^+/Li) p-type electrode materials^{S9-S10}.

We have measured the cyclic voltammograms of tris(4-ethynylphenyl)-amine (TEPA) and triphenylamine (TPA) in DMF, as shown in **Fig. S45**. The potentials of both compounds are above 1.1V (vs. Ag/AgCl), which are much higher than the potentials of viologens (about -0.3V). According to the CV profiles and previous

reported work^{S11}, the capacity contribution for triphenylamine units in our polymer can be negligible.

However, we cannot totally rule out the capacity contribution of TEPA units in **P1**. Because TEPA part may contribute partial capacity due to the superlithium process during the cycling. In addition, the incorporation of electron-donating TEPA accelerates the charge transfer process, which is one of the most promising reasons for the excellent electrochemistry of **P1**.

Table S1. Crystal data and structure refinement for **3** (CCDC 2071615).

Identification code	3
Empirical formula	C ₁₅ H ₁₁ F ₃ N ₂ O ₄ S ₂
Formula weight	404.38
Temperature/K	153.0
Crystal system	monoclinic
Space group	C2/c
a/Å	16.4424(12)
b/Å	10.2099(8)
c/Å	20.8080(15)
α /°	90
β /°	110.745(2)
γ /°	90
Volume/Å ³	3266.7(4)
Z	8
ρ_{calc} /cm ³	1.644
μ /mm ⁻¹	3.515
F(000)	1648.0
Crystal size/mm ³	0.5 × 0.4 × 0.3
Radiation	CuK α (λ = 1.54178)
2 Θ range for data collection/°	9.088 to 136.608
Index ranges	-19 ≤ h ≤ 19, -12 ≤ k ≤ 12, -25 ≤ l ≤ 25
Reflections collected	24564
Independent reflections	2978 [R_{int} = 0.0473, R_{sigma} = 0.0271]
Data/restraints/parameters	2978/0/236
Goodness-of-fit on F ²	1.054
Final R indexes [$I \geq 2\sigma(I)$]	R_1 = 0.0276, wR_2 = 0.0763
Final R indexes [all data]	R_1 = 0.0350, wR_2 = 0.0781
Largest diff. peak/hole / e Å ⁻³	0.32/-0.33

Table S2. Bond Lengths for **3**.

Atom	Atom	Length/Å	Atom	Atom	Length/Å
S1	O1	1.4376(11)	N2	C7	1.4466(18)
S1	O2	1.4425(11)	N2	C8	1.3583(18)
S1	O3	1.4425(10)	C1	C2	1.367(2)
S1	C14	1.8298(17)	C1	C3	1.3920(19)
S2	C5 ¹	1.7572(14)	C3	C4	1.4011(19)
S2	C9	1.7194(14)	C3	C5	1.454(2)
F1	C14	1.332(2)	C4	C8	1.369(2)
F2	C14	1.331(2)	C6	C10	1.395(2)
F3	C14	1.3300(19)	C6	C11	1.376(2)
O4	C10	1.3618(18)	C7	C11	1.395(2)
O4	C15	1.436(2)	C7	C12	1.386(2)
N1	C5	1.3164(18)	C9	C9 ¹	1.382(3)
N1	C9	1.3527(19)	C10	C13	1.389(2)
N2	C2	1.3552(18)	C12	C13	1.387(2)

Table S3 Bond Angles for **3**.

Atom	Atom	Atom	Angle/°	Atom	Atom	Atom	Angle/°
O1	S1	O2	114.81(6)	C11	C6	C10	120.61(13)
O1	S1	O3	115.37(7)	C11	C7	N2	120.68(12)
O1	S1	C14	103.87(7)	C12	C7	N2	119.21(12)
O2	S1	C14	102.89(8)	C12	C7	C11	120.03(13)
O3	S1	O2	114.92(7)	N2	C8	C4	121.35(13)
O3	S1	C14	102.48(7)	N1	C9	S2	132.55(11)
C9	S2	C5 ¹	87.88(7)	N1	C9	C9 ¹	118.06(16)
C10	O4	C15	117.25(13)	C9 ¹	C9	S2	109.38(14)
C5	N1	C9	108.11(12)	O4	C10	C6	115.80(13)
C2	N2	C7	119.84(11)	O4	C10	C13	124.57(13)
C2	N2	C8	119.51(12)	C13	C10	C6	119.63(14)
C8	N2	C7	120.47(11)	C6	C11	C7	119.57(13)
C2	C1	C3	120.44(13)	C7	C12	C13	120.22(13)
N2	C2	C1	121.04(13)	C12	C13	C10	119.84(14)
C1	C3	C4	117.72(13)	F1	C14	S1	110.99(12)
C1	C3	C5	121.77(13)	F2	C14	S1	111.43(13)
C4	C3	C5	120.48(13)	F2	C14	F1	107.22(13)
C8	C4	C3	119.79(13)	F3	C14	S1	111.61(10)
N1	C5	S2 ¹	116.56(11)	F3	C14	F1	107.74(15)
N1	C5	C3	122.58(12)	F3	C14	F2	107.65(14)
C3	C5	S2 ¹	120.83(10)				

Table S4. Torsion Angles for **3**.

A	B	C	D	Angle/°	A	B	C	D	Angle/°
O1	S1	C14	F1	179.58(11)	C4	C3	C5	N1	3.0(2)
O1	S1	C14	F2	60.16(12)	C5 ¹	S2	C9	N1	179.53(14)
O1	S1	C14	F3	-60.23(15)	C5 ¹	S2	C9	C9 ¹	0.33(13)
O2	S1	C14	F1	-60.43(13)	C5	N1	C9	S2	-179.83(11)
O2	S1	C14	F2	-179.85(11)	C5	N1	C9	C9 ¹	-0.7(2)
O2	S1	C14	F3	59.77(14)	C5	C3	C4	C8	-174.91(13)
O3	S1	C14	F1	59.13(13)	C6	C10	C13	C12	-2.7(2)
O3	S1	C14	F2	-60.29(13)	C7	N2	C2	C1	-172.86(12)
O3	S1	C14	F3	179.33(13)	C7	N2	C8	C4	172.18(13)
O4	C10	C13	C12	177.57(15)	C7	C12	C13	C10	1.5(2)
N2	C7	C11	C6	173.57(13)	C8	N2	C2	C1	2.3(2)
N2	C7	C12	C13	-175.36(14)	C8	N2	C7	C11	154.76(13)
C1	C3	C4	C8	3.3(2)	C8	N2	C7	C12	-28.55(19)
C1	C3	C5	S2 ¹	2.99(18)	C9	N1	C5	S2 ¹	0.39(15)
C1	C3	C5	N1	-175.10(12)	C9	N1	C5	C3	178.57(12)
C2	N2	C7	C11	-30.13(19)	C10	C6	C11	C7	1.9(2)
C2	N2	C7	C12	146.56(14)	C11	C6	C10	O4	-179.30(13)
C2	N2	C8	C4	-3.0(2)	C11	C6	C10	C13	0.9(2)
C2	C1	C3	C4	-3.9(2)	C11	C7	C12	C13	1.4(2)
C2	C1	C3	C5	174.23(13)	C12	C7	C11	C6	-3.1(2)
C3	C1	C2	N2	1.2(2)	C15	O4	C10	C6	177.18(16)
C3	C4	C8	N2	0.1(2)	C15	O4	C10	C13	-3.1(2)
C4	C3	C5	S2 ¹	-178.89(10)					

Table S5. Emission quantum yield of **1-4** in different solvents.^a

	CH ₂ Cl ₂	THF	CH ₃ CN	MeOH	DMF
1	0.60	0.023	0.67	0.51	n.d. ^b
2	0.36	0.019	0.48	0.43	n.d. ^b
3	0.0045	0.0003	n.d.	n.d.	n.d. ^b
4	n.d.	5.2	0.62	0.85	0.0033

a. The absolute quantum yields were measured by the integrating sphere method.

b. Signal was too weak to be detected.

Table S6. The optimized structures and HOMO/LUMO for **1-4**.

All DFT calculations were carried out using the Gaussian 09 program package. The geometries of **1-4** were fully optimized at the B3LYP/6-31G(d) level of theory in CH₃CN utilizing the polarizable continuum model (PCM) solvation model for compounds **1-4**.

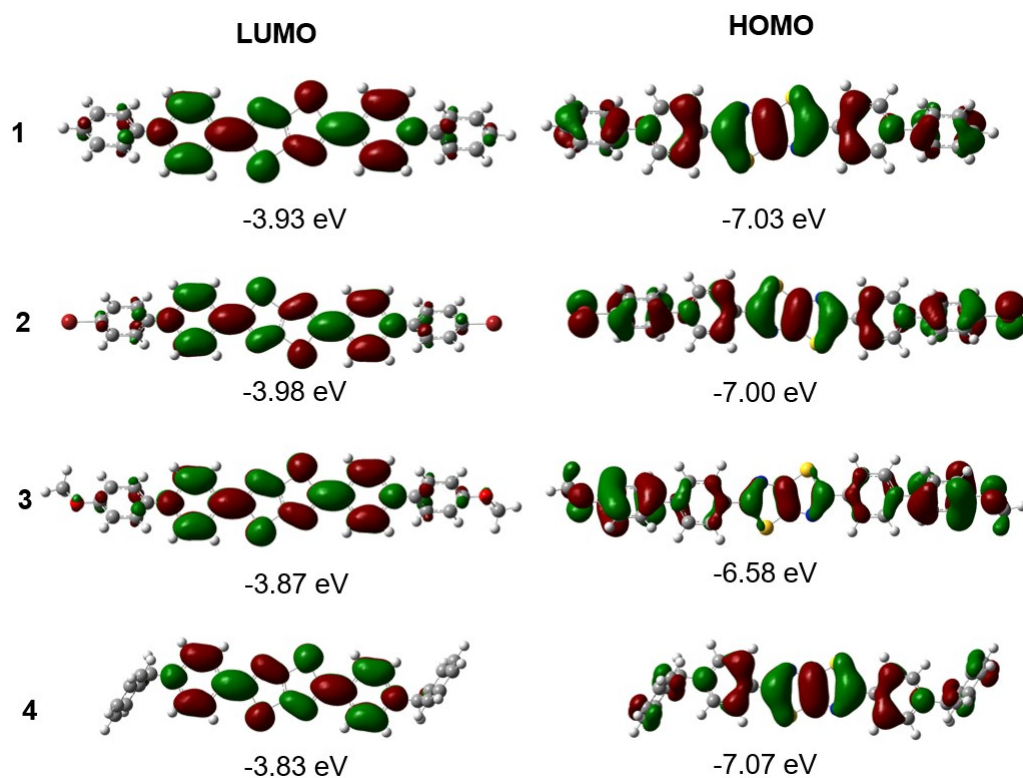


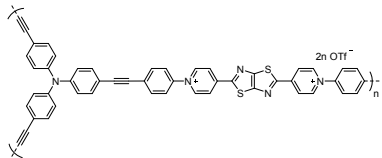
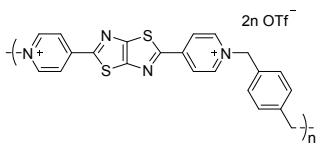
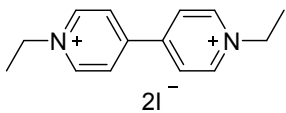
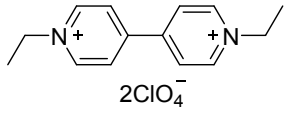
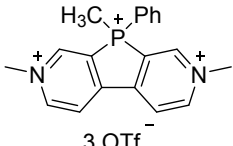
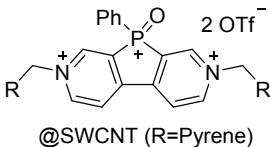
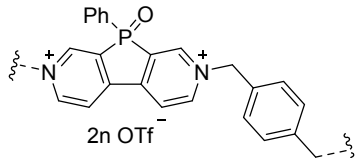
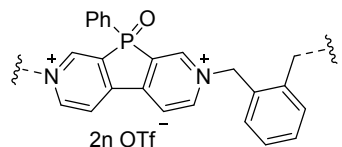
Table S7. Capacity retention of **P1**, **P2-Br** and **P2** in different cycles.

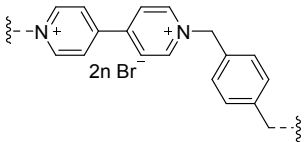
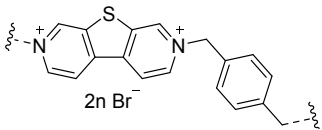
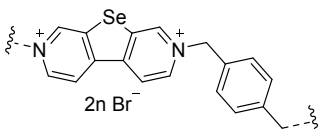
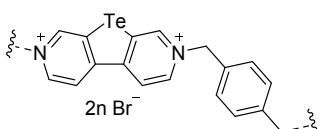
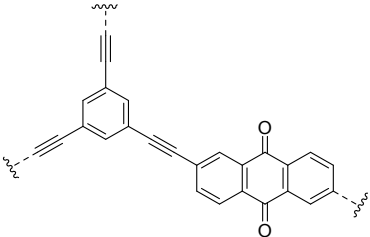
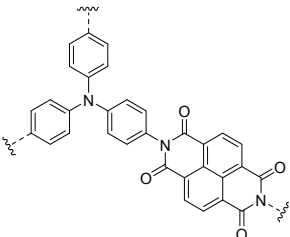
Sample	Current density (mA g ⁻¹)	Discharge capacity (mAh g ⁻¹)		Capacity retention (%)
		2nd	1000th	
P1	800	357.9	358.8	100.2
	1000	327.5	326.9	99.8
P2-Br	800	415.4	120.8	29.1
P2	800	379.6	105.1	27.7

Table S8. Simulation parameters obtained by fitting the impedance spectra to the equivalent circuit.

Sample	State	R _s	R _i	R _{ct}
P1	Fresh	1.579	-	77.22
	after 1000 cycles	3.965	14.46	25.04
P2	Fresh	1.296	-	210.80
	after 1000 cycles	2.840	19.47	59.40

Table S9. Cycling performance comparison of **P1** and other organic electrodes.

Materials	Electrode Composition	Voltage Range (V vs Li/Li ⁺)	Capacity and Capacity Retention	Reference
	active materials: ECP-600JD: PVDF=6:3:1	0.005-3.0	358.8 mAh g ⁻¹ , 100.2% (at 800 mA g ⁻¹ after 1000 cycles)	This work
	active materials: ECP-600JD: PVDF=6:3:1	0.005-3.0	105.1 mAh g ⁻¹ , 27.7% (at 800 mA g ⁻¹ after 1000 cycles)	This work
	active materials: Super P: PVDF=8:1:1	1.6-4.0	218 mAh g ⁻¹ , 96% (at 0.5C after 200 cycles)	S12
	active materials: Super P: PVDF=8:1:1	1.6-3.0	~125 mAh g ⁻¹ , 98% (at 0.5C after 200 cycles)	S12
	active materials: SWCNT: PVDF=4:4:2	2.0-4.5	~25 mAh g ⁻¹ , ~100% (at 1C after 120 cycles)	S13
	active materials: PVDF=8:2	1.95-3.5	53 mAh g ⁻¹ , 110% (at 1C after 500 cycles)	S14
	active materials: Norit 100: PVDF=4:9:3	1.8-3.1	60 mAh g ⁻¹ , 82% (at 1C after 70 cycles)	S15
	active materials: Norit 100: PVDF=4:9:3	1.8-3.2	40 mAh g ⁻¹ , 84% (at 1.5C after 150 cycles)	S16

	active materials: carbon blank: PVDF=6:3:1	0.001-3.0	326 mAh g ⁻¹ , 66% (at 100 mA g ⁻¹ after 40 cycles)	S16
	active materials: carbon blank: PVDF=6:3:1	0.001-3.0	416 mAh g ⁻¹ , 57% (at 100 mA g ⁻¹ after 40 cycles)	S16
	active materials: carbon blank: PVDF=6:3:1	0.001-3.0	462 mAh g ⁻¹ , 72% (at 100 mA g ⁻¹ after 40 cycles)	S16
	active materials: carbon blank: PVDF=6:3:1	0.001-3.0	502 mAh g ⁻¹ , 73% (at 100 mA g ⁻¹ after 40 cycles)	S16
	active materials: MWCNTs: PVDF=5:4:1	1.5-3.5	46.7 mAh g ⁻¹ , 57% (at 2C after 9000 cycles)	S17
	active materials: acetylene black: PVDF=4:5:1	1.5-4.2	125 mAh g ⁻¹ , 87% (at 0.1C after 100 cycles)	S18

Reference:

- S1.** Woodward, A. N.; Kolesar, J. M.; Hall, S. R.; Saleh, N. A.; Jones, D. S.; Walter, M. G. Thiazolothiazole Fluorophores Exhibiting Strong Fluorescence and Viologen-Like Reversible Electrochromism. *J. Am. Chem. Soc.* **2017**, *139* (25), 8467-8473.
- S2.** Bielawski, M.; Zhu, M.; Olofsson, B. Efficient and General One-Pot Synthesis of Diaryliodonium Triflates: Optimization, Scope and Limitations. *Adv. Synth. Catal.* **2007**, 349, 2610-2618.
- S3.** Corte, D. A. D.; Caillon, G.; Jordy, C.; Chazalviel, J.; Rosso, M.; Ozanam, F. Spectroscopic Insight into Li-Ion Batteries during Operation: An Alternative Infrared Approach. *Adv. Energy Mater.*, **2016**, *6* (2), 1501768.
- S4.** Zhao, C.; Chen, Z.; Wang, W.; Xiong, P.; Li, B.; Li, M.; Yang, J.; Xu, Y. In Situ Electropolymerization Enables Ultrafast Long Cycle Life and High-Voltage Organic Cathodes for Lithium Batteries. *Angew. Chem. Int. Ed.* **2020**, *59*(29), 11992-11998.
- S5.** Man, Z.; Li, P.; Zhou, D.; Zang, R.; Wang, S.; Li, P.; Liu, S.; Li, X.; Wu, Y.; Liang X.; Wang G. High-performance lithium-organic batteries by achieving 16 lithium storage in poly(imine-anthraquinone). *J. Mater. Chem. A*, **2019**, *7*(5), 2368-2375.
- S6.** Jiang, Q.; Xiong, P.; Liu, J.; Xie, Z.; Wang, Q.; Yang, X.-Q.; Hu, E.; Cao, Y.; Sun, J.; Xu, Y.; Chen, L. A Redox-Active 2D Metal–Organic Framework for Efficient Lithium Storage with Extraordinary High Capacity. *Angew. Chem. Int. Ed.*, **2020**, *59*(13), 5273-5277.
- S7.** Lu, Y.; Chen, J. Prospects of organic electrode materials for practical lithium batteries. *Nat. Rev. Chem.*, **2020**, *4*, 127-142.
- S8.** Sun, T.; Xie, J.; Guo, W.; Li, D.-S.; Zhang, Q. Covalent–Organic Frameworks: Advanced Organic Electrode Materials for Rechargeable Batteries. *Adv. Energy Mater.*, **2020**, *10*(19), 1904199.
- S9.** Su, C.; He, H.; Xu, L.; Zhao, K.; Zheng, C.; Zhang, C. A mesoporous conjugated polymer based on a high free radical density polytriphenylamine derivative: its preparation and electrochemical performance as a cathode material for Li-ion batteries. *J. Mater. Chem. A*, **2017**, *5*(6), 2701-2709.
- S10.** Choi, J.; Kim, E. S.; Ko, J. H.; Lee, S. M.; Kim, H. J.; Ko, Y.-J.; Son, S. U. Hollow and microporous triphenylamine networks post-modified with TCNE for enhanced organocathode performance. *Chem. Commun.*, **2017**, *53*(62), 8778-8781.
- S11.** Wang, G.; Chandrasekhar, N.; Biswal, B. P.; Becker, D.; Paasch, S.; Brunner, E.; Addicoat, M.; Yu, M.; Berger, R.; Feng, X. A Crystalline, 2D Polyarylimide Cathode for Ultrastable and Ultrafast Li Storage. *Adv. Mater.*, **2019**, *31*(28), 1901478.
- S12.** Ma, T.; Liu, L.; Wang, J.; Lu, Y.; Chen, J. Charge Storage Mechanism and Structural Evolution of Viologen Crystals as the Cathode of Lithium Batteries. *Angew. Chem. Int. Ed.* **2020**, *59* (28), 11533-11539.
- S13.** Bridges, C. R.; Borys, A. M.; Béland, V. A.; Gaffen, J. R.; Baumgartner, T. Phosphoryl- and phosphonium-bridged viologens as stable two- and three-electron acceptors for organic electrodes. *Chem. Sci.* **2020**, *11* (38), 10483-10487.

- S14.** Bridges, C. R.; Stolar, M.; Baumgartner, T. Phosphaviologen-Based Pyrene-Carbon Nanotube Composites for Stable Battery Electrodes. *Batteries Supercaps* **2019**, 3 (3), 268-274.
- S15.** Stolar, M.; Reus, C.; Baumgartner, T., Xylene-Bridged Phosphaviologen Oligomers and Polymers as High-Performance Electrode-Modifiers for Li-Ion Batteries. *Adv. Energy Mater.* **2016**, 6 (20), 1600944.
- S16.** Li, G.; Zhang, B.; Wang, J.; Zhao, H.; Ma, W.; Xu, L.; Zhang, W.; Zhou, K.; Du, Y.; He, G. Electrochromic Poly(chalcogenoviologen)s as Anode Materials for High-Performance Organic Radical Lithium-Ion Batteries. *Angew. Chem. Int. Ed.* **2019**, 58 (25), 8468-8473.
- S17.** Molina, A.; Patil, N.; Ventosa, E.; Liras, M.; Palma, J.; Marcilla, R. New Anthraquinone-Based Conjugated Microporous Polymer Cathode with Ultrahigh Specific Surface Area for High-Performance Lithium-Ion Batteries. *Adv. Funct. Mater.* **2019**, 30 (6), 1908074
- S18.** Chen, S.; Jia, T.; Zhou, G.; Zhang, C.; Hou, Q.; Wang, Y.; Luo, S.; Shi, G.; Zeng, Y., A Cross-Linked Triphenylamine-Based Polymer Cathode Material with Dual Anion-Cation Reversible Insertion for Lithium Ion Battery. *J. Electrochem. Soc.* **2019**, 166 (12), A2543-A2548.